

Colossal anomalous Nernst effect in a correlated noncentrosymmetric kagome ferromagnet

T. Asaba^{1*}, V. Ivanov², S. M. Thomas¹, S.Y. Savrasov²,
J. D. Thompson¹, E. D. Bauer¹, F. Ronning^{3*}

¹*Materials Physics and Applications Division,
Los Alamos National Laboratory, NM, 87545 USA*

²*Department of Physics,
University of California,
Davis, CA 95616, USA*

³*Institute for Materials Science,
Los Alamos National Laboratory, NM, 87545 USA*

(Dated: April 20, 2021)

Abstract

Analogous to the Hall effect, the Nernst effect is the generation of a transverse voltage due to a temperature gradient in the presence of a perpendicular magnetic field. The Nernst effect has promise for thermoelectric applications and as a probe of electronic structure. In magnetic materials, a so-called anomalous Nernst effect (ANE) is possible in zero magnetic field. Here we report a colossal ANE reaching $23 \mu\text{V}/\text{K}$ in the ferromagnetic metal $\text{UCo}_{0.8}\text{Ru}_{0.2}\text{Al}$. Uranium's $5f$ electrons provide strong electronic correlations that lead to narrow bands, which are a known route to producing a large thermoelectric response. Additionally, the large nuclear charge of uranium generates strong spin-orbit coupling, which produces an intrinsic transverse response in this material due to the Berry curvature associated with the relativistic electronic structure. Theoretical calculations show that at least 148 Weyl nodes and two nodal lines exist within ± 60 meV of the Fermi level in $\text{UCo}_{0.8}\text{Ru}_{0.2}\text{Al}$. This work demonstrates that magnetic actinide materials can host strong Nernst and Hall responses due to their combined correlated and topological nature.

Introduction

Because electrons carry both heat and charge, the transport of one is necessarily related to the other. Thermoelectric applications aim to exploit this fact by converting heat or charge flow into electric voltages or temperature gradients (1, 2). In the presence of a magnetic field transverse responses are possible. It has been argued that the transverse geometry allows one to convert heat into electrical energy much more efficiently than the conventional longitudinal geometry (1, 3, 4). In conventional materials, however, the amplitude of the transverse anomalous Nernst effect (ANE) has been too small to realize practical thermoelectric devices.

Recently, it has been recognized that the Berry curvature associated with the Bloch waves of electrons generates an additional and potentially very large transverse response in magnetic materials (5–9). This is exemplified by the full-Heusler ferromagnet Co_2MnGa whose ANE at room temperature is $6 \mu\text{V}/\text{K}$ and reaches to a record $8 \mu\text{V}/\text{K}$ at $T = 400$ K (3). This value is larger than typical ferromagnets, and theoretical calculations reveal that the large ANE is a consequence of the intrinsic Berry curvature contribution. After the triumph of Co_2MnGa , a natural question arises: Can one further enhance or maximize the size of the ANE for applications or due to fundamental constraints? In this paper, we examine a uranium compound, which has multiple favorable attributes for enhancing the

Berry curvature and ANE, and indeed we find an ANE, which is even four times larger than found in Co₂MnGa.

The Nernst Effect is related to the thermoelectric ($\bar{\alpha}$) and conductivity ($\bar{\sigma}$) tensors through the expression $S_{xy} = -E_y/\nabla_x T = (\sigma_{xx}\alpha_{xy} - \sigma_{xy}\alpha_{xx})/(\sigma_{xx}^2 + \sigma_{xy}^2)$. The transverse contribution to the thermoelectric and conductivity tensors is directly connected to the Berry curvature Ω_B through

$$\sigma_{xy} = -\frac{e^2}{\hbar} \int_{BZ} \frac{d^3k}{(2\pi)^3} f(k)\Omega_B(k) \quad (1)$$

$$\alpha_{xy} = \frac{ek_B}{\hbar} \int_{BZ} \frac{d^3k}{(2\pi)^3} s(k)\Omega_B(k) \quad (2)$$

where k_B is Boltzmann's constant, e is the charge of an electron, \hbar is Planck's constant h divided by 2π , $f(k)$ is the Fermi-Dirac distribution function, $s(k) = -f(k)\ln(f(k)) - (1 - f(k))\ln(1 - f(k))$, and \int_{BZ} is the integration over the Brillouin zone. At low temperatures, these two quantities are related through the Mott formula (10, 11).

An examination of these equations reveals that large Berry curvatures and small Fermi energies E_F will generate large Hall and Nernst effects, in general. As elaborated on below, to enhance the Berry curvature contribution to the ANE and AHE we therefore look for a system with the following properties: (1) a large spin-orbit coupling, (2) strong electronic correlations, (3) ferromagnetic order, and (4) a kagome lattice structure.

The Berry curvature depends strongly on the spin-orbit coupling (SOC). Increasing the strength of the SOC increases the potential occurrence of band inversions, which generate regions of potentially diverging Berry curvature in the Brillouin zone. Depending on the symmetry of the inverted bands, nodal lines and/or Dirac or Weyl nodes may appear. Generally, the strength of the SOC increases with increasing atomic number, and hence we look for materials near the bottom of the periodic table.

To maximize the effects of larger SOC requires multiple bands to reside in the vicinity of the Fermi energy. This can be accomplished through strong electronic correlations, which will shift multiple band crossing points closer to the Fermi energy, thereby enhancing the Berry curvature. Furthermore, the renormalized band structures due to electronic correlations lead to smaller effective Fermi energies, which is known to promote large Seebeck and Nernst responses (12, 13). The need for both strong correlations and large SOC leads us naturally to heavy fermion systems composed of $4f$ and $5f$ elements.

Without broken time-reversal symmetry a transverse Hall or Nernst response is identically zero. Hence, in the absence of an applied magnetic field, magnetic order is required for a finite ANE or AHE. Although possible in a system with antiferromagnetic order (8, 9, 14, 15), the requisite absence of symmetries is guaranteed in a ferromagnetic system.

In a system with antiferromagnetic interactions, magnetic frustration present in a kagome lattice can lead to additional band renormalization. Though magnetic frustration is presumably absent in a ferromagnetic material, the unrenormalized hopping on a kagome lattice coincidentally produces one flat band. Perhaps this explains in part, why large AHE and ANE responses have been recently observed in a number of kagome compounds (6, 16–19).

In our exploration of materials we found that the layered distorted kagome lattice system $\text{UCo}_{1-x}\text{Ru}_x\text{Al}$ in the ZrNiAl structure type (shown in Fig. 1A) satisfies all the above criteria. Additionally, the crystal structure is non-centrosymmetric, which can generate pairs of Weyl nodes with opposite chiralities. By themselves such Weyl nodes do not contribute to the AHE and ANE, but they can be further split by the magnetic order. Both parent compounds UCoAl and URuAl are paramagnetic, but much of their solid solution $\text{UCo}_{1-x}\text{Ru}_x\text{Al}$ is ferromagnetic (20, 21). Members of the entire alloy series show relatively large Sommerfeld coefficients γ of ~ 50 mJ/mol K^2 (21–24), indicating that charge carriers are moderately heavy. Magnetic X-ray and photoemission measurements also certify the presence of electronic correlations (25, 26). Furthermore, previous work has shown significant anomalous Hall conductivity (AHC) for dopings close to the quantum-phase transition (21). Here we examine $x=0.2$ with a T_C of 56 K, close to the optimal value in the series.

Results

Our spin-polarized theoretical calculations including spin-orbit coupling support our initial conjecture. A partial density of states of $\text{UCo}_{0.8}\text{Ru}_{0.2}\text{Al}$ shown in Fig. 1B reveals a narrow band of uranium f -states dominating the electronic structure near E_F . Electronic correlations are expected to further reduce this bandwidth (24). The magnitude of the calculated anomalous Hall conductivity due to the Berry curvature is found to be $\sim 2,000$ $\Omega^{-1}\text{cm}^{-1}$, though the value, and sign, is highly sensitive to details of the electronic structure (24). The origin of this large AHC is due to the dominant flat $5f$ uranium bands creating a remarkable number of topological features close to E_F . Fig. 1C shows the location of a subset of the Weyl nodes in the Brillouin zone that are within ± 60 meV of the Fermi level. There are at least 148 Weyl points, which is by far larger than other Weyl materials. There

exist both type I and type II Weyl nodes, as well as a few that are proximate to a Lifshitz transition between the two types (See Fig. 1D). Such a "quantum-critical" Weyl node was argued to be the origin of the large Nernst response in Co_2MnGa (3). We additionally find two topological nodal lines close to E_F within the σ_z mirror plane (Fig. 1C). Such nodal lines arise at the crossing of bands belonging to distinct irreducible representations of the mirror plane point group and are protected against perturbations by the existence of mirror symmetry. While these nodal lines are significant sources of Berry curvature, they will not contribute to Ω_{xy}^z . We note that first principles calculations of the electronic structure of uranium compounds is notoriously challenging, but the main observation of an incredibly large number of Weyl nodes and Berry curvature found here is independent of the details of the electronic structure (see (24)).

The temperature dependence of the longitudinal resistivity ρ_{xx} and the Seebeck coefficient S_{xx} of a single crystal of $\text{UCo}_{0.8}\text{Ru}_{0.2}\text{Al}$ is shown in Fig. 2A and B. A kink is observed in both ρ_{xx} and S_{xx} at the ferromagnetic $T_C = 56$ K. The sample is a bad metal as reflected by the large residual resistivity ($105 \mu\Omega\text{cm}$). A longitudinal conductivity σ_{xx} of $\sim 9,500 \Omega^{-1}\text{cm}^{-1}$, which falls within the moderately dirty regime where $\sigma_{xx} = 3 \times 10^3 - 5 \times 10^5 \Omega^{-1}\text{cm}^{-1}$, is the first indication that the transverse transport will be dominated by the intrinsic contribution (27). In the $T=0$ limit the S_{xx}/T gives a value of $0.9 \mu\text{V}/\text{K}^2$. This suggests a Fermi temperature of ~ 470 K (12), consistent with a Fermi temperature of 930 K estimated by specific heat (24). We also note that the ratio of the experimental Sommerfeld coefficient to the computed value based on density functional theory implies a mass renormalization of ~ 3 (24).

The temperature and field dependent magnetization of $\text{UCo}_{0.8}\text{Ru}_{0.2}\text{Al}$ is shown in Fig. 2C and D. The system shows very strong Ising-type magnetic anisotropy, with the easy axis along the c -axis. The saturation magnetic moment of $0.59 \mu_B/\text{U}$ is consistent with a previous study (20) and implies that the uranium $5f$ electrons are rather strongly hybridized with ligand electrons. A small field of $B = 0.1$ T is enough to polarize the magnetic moments during field cooling (FC). Thus, we take the transverse responses (Hall, Nernst and Righi–Leduc effects) with FC and $B = 0.1$ T conditions, which is small enough to render the ordinary contributions as negligible.

The field and temperature dependence of the Hall, Nernst and Righi–Leduc effects are shown in Figs. 3 A-F. For the field dependence, they all show a step-like behavior similar to

the magnetization. The saturated response at high fields in the ordered state confirms that the transverse effects are dominated by the anomalous contribution and the ordinary component is negligibly small. Consequently, the transverse response discussed in the remainder of the paper implicitly refers to the anomalous component. The vanishing transverse response as the temperature exceeds T_C is also consistent with this picture.

The anomalous Hall effect of $\text{UCo}_{0.8}\text{Ru}_{0.2}\text{Al}$ is found to be very large, as shown in Figs. 3A and 3B. At $T = 40$ K ρ_{xy} is $-16 \mu\Omega\text{cm}$, which decreases to $-11 \mu\Omega\text{cm}$ at $T = 2$ K, corresponding to a conductivity of $\sigma_{xy} = 980/\Omega\text{cm}$. These values are similar to that of Co_2MnGa and $\text{Co}_3\text{Sn}_2\text{S}_2$, and among the largest values for ferromagnetic metals (3, 16).

Next, we display our primary result - a colossal anomalous Nernst effect. While the anomalous Hall resistivity is as large as in Co_2MnGa and $\text{Co}_3\text{Sn}_2\text{S}_2$, more surprisingly, the anomalous Nernst effect is found to be colossal in $\text{UCo}_{0.8}\text{Ru}_{0.2}\text{Al}$, reaching $23 \mu\text{V}/\text{K}$ at $T = 40$ K (Fig. 3 C and D). To the best of our knowledge, this is approximately 3-4 times larger than the current record value of $6-8 \mu\text{V}/\text{K}$ held by Co_2MnGa (3). Furthermore, in $\text{UCo}_{0.8}\text{Ru}_{0.2}\text{Al}$ the magnitude of S_{xy} at 40 K is comparable to the Seebeck coefficient. Consequently, the anomalous Nernst angle $\tan(\theta_N) = |S_{xy}/S_{xx}|$ reaches 0.92 at 41 K, where both S_{xx} and S_{xy} have extrema with values of $-25.5 \mu\text{V}/\text{K}$ and $23.5 \mu\text{V}/\text{K}$, respectively.

Fig. 3 E and F displays the anomalous thermal Hall conductivity κ_{xy} of $\text{UCo}_{0.8}\text{Ru}_{0.2}\text{Al}$ as a function of field and temperature. To check the validity of the anomalous Wiedemann-Franz (WF) law $L_0 = \frac{\kappa_{xy}}{\sigma_{xy}T}$ where $L_0 = \frac{\pi^2 k_B^2}{3e^2} = 2.44 \times 10^{-8} \text{ W}\Omega/\text{K}^2$, we compared κ_{xy} with $L_0\sigma_{xy}T$ (Fig. 3 F). We find that they overlap each other very well and thus the WF law is valid. The validity of a transverse WF law indicates that the anomalous transverse entropy and charge flow are governed by the intrinsic contribution from the Berry curvature (8, 15).

Discussion

The anomalous Hall conductivity as a function of T/T_C for a variety of materials with large transverse responses in heat and charge (15, 28–30) is shown in Fig. 4 A. The AHC of $\text{UCo}_{0.8}\text{Ru}_{0.2}\text{Al}$ is almost temperature-independent below $T = 0.5 T_C$. This implies that the AHC is independent of scattering rate, which is additional support that the intrinsic contribution dominates the transverse response in this system. At $T = 2$ K, $|\sigma_{xy}|$ reaches $980/\Omega\text{cm}$ in $\text{UCo}_{0.8}\text{Ru}_{0.2}\text{Al}$, which is comparable to Co_2MnGa , one of the largest intrinsic AHC known. The AHC from SrRuO_3 and Mn_3Ge are almost one order of magnitude smaller than that of $\text{UCo}_{0.8}\text{Ru}_{0.2}\text{Al}$. The anomalous Peltier conductivity α_{xy} as a function of T/T_C

for these materials is shown in Fig. 4 B. The Peltier coefficient is the sum of two contributions $\sigma_{xx}S_{xy}$ and $\sigma_{xy}S_{xx}$. In $\text{UCo}_{0.8}\text{Ru}_{0.2}\text{Al}$, $\sigma_{xx}S_{xy} \gg \sigma_{xy}S_{xx}$ (see SI). In sharp contrast to the fact that σ_{xy} of $\text{UCo}_{0.8}\text{Ru}_{0.2}\text{Al}$ is comparable to that of Co_2MnGa and $\text{Co}_3\text{Sn}_2\text{S}_2$, α_{xy} of $\text{UCo}_{0.8}\text{Ru}_{0.2}\text{Al}$ is roughly 3-4 times larger than that of Co_2MnGa , the current record holder for α_{xy} , and $\text{Co}_3\text{Sn}_2\text{S}_2$. α_{xy} of SrRuO_3 and Mn_3Ge are significantly smaller.

Why is α_{ij} so large in $\text{UCo}_{0.8}\text{Ru}_{0.2}\text{Al}$? In Fig. 4 C we plot the maximal value of $|\alpha_{ij}|$ vs λ_{SOC} for various compounds. λ_{SOC} is estimated from atomic calculations of the magnetic element (31, 33). Despite this very rough estimate for the strength of the SOC in these materials, Fig. 4 C supports our original conjecture that a large spin-orbit coupling increases the possibility for more band inversions, which can create a large Berry curvature contribution to anomalous transverse response functions (34).

A large SOC alone, however, is insufficient to explain the remarkable properties of $\text{UCo}_{0.8}\text{Ru}_{0.2}\text{Al}$, because the maximal contribution from any pair of bands to the AHE is e^2/hc , where c is the c -axis lattice constant, and in this limit one expects a vanishing ANE. Instead our electronic structure calculations shown in Fig. 1 reveal that there are many bands in the vicinity of the Fermi energy. This is a consequence of the nature of the $5f$ electrons in uranium. Furthermore, electronic correlations will further renormalize the bands leading to smaller effective Fermi energies, which is known to enhance thermoelectric properties (12). Notably, the Sommerfeld coefficient of the heat capacity γ is significantly larger for $\text{UCo}_{0.8}\text{Ru}_{0.2}\text{Al}$ (41 mJ/mol K²) compared to Co_2MnGa (12 mJ/mol K²) (3). Thus, it is the combination of the small effective Fermi energy and the large SOC that leads to multiple topological features within the energy window set by the SOC and that enables the remarkably large values of both σ_{ij} and α_{ij} in $\text{UCo}_{0.8}\text{Ru}_{0.2}\text{Al}$.

It is interesting to ask, which specific features of the electronic structure are most responsible for the large anomalous Nernst effect in $\text{UCo}_{0.8}\text{Ru}_{0.2}\text{Al}$. $\text{UCo}_{0.8}\text{Ru}_{0.2}\text{Al}$ crystallizes in the non-symmorphic space group 189. From basic symmetry considerations this space group has been argued to possess a variety of interesting topological features, including Weyl nodes(35–38), nodal lines (39–42), and triple points(43, 44). All of these features appear in our electronic structure calculations (24). Notably, one set of critically tilted Weyl points lies 25 meV above E_f , corresponding to a doping of $x \sim 0.07$ in the rigid band picture. For this set of Weyl nodes we compute values of $\sigma_{xy} \sim 1200$ ($\Omega \text{ cm}$)⁻¹ and $\alpha_{xy} \sim 20$ A(K m)⁻¹ at that energy, which may be shifted as a consequence of electronic correlations. Another

possibility is that electronic correlations pin the Weyl nodes to the chemical potential as has been suggested in some Weyl-Kondo semimetals (45). Additional measurements, such as ARPES, will be required to confirm the identity of the most relevant topological features in $\text{UCo}_{0.8}\text{Ru}_{0.2}\text{Al}$.

Finally, we consider the relationship between σ_{ij} and α_{ij} . From the Mott relation, which is valid in the $T = 0$ limit, a large α_{ij}/T implies that σ_{ij} can be enhanced by appropriately tuning the chemical potential. As temperature is increased the relationship between σ_{ij} and α_{ij} is less straight forward. Behnia *et al.* have argued, however, that the ratio of α_{ij}/σ_{ij} is bounded by the ratio of natural units $k_B/e = 86 \mu\text{V}/\text{K}$, which reflects the fact that the Peltier coefficient represents the transport of entropy, while the Hall coefficient represents the transport of charge (28). For $\text{UCo}_{0.8}\text{Ru}_{0.2}\text{Al}$ α_{ij}/σ_{ij} reaches $170 \mu\text{V}/\text{K}$ at $T = 47 \text{ K}$, as shown in Fig. 4 D. This supports the notion that multiple bands are simultaneously contributing to the large Nernst response in $\text{UCo}_{0.8}\text{Ru}_{0.2}\text{Al}$.

In conclusion, we have found a colossal anomalous Nernst effect in $\text{UCo}_{0.8}\text{Ru}_{0.2}\text{Al}$. The simultaneous presence of strong spin-orbit coupling and electronic correlations drives narrow bands leading to a gigantic Nernst response and presents an exciting blueprint for how to develop magnetic topological metals for thermoelectric applications.

Materials and Methods

A single crystal of nominal composition $\text{UCo}_{0.8}\text{Ru}_{0.2}\text{Al}$ was grown by the Czochralski method in a tri-arc furnace. The crystal structure was confirmed to have the $P\bar{6}2m$ (#189) space group with the ZrNiAl structure type. Powder and single crystal diffraction was performed to confirm the crystal structure and the phase purity of the samples. The sample was oriented and the quality was further checked by the X-ray Laue method with a photo-sensitive detector in backscattering geometry. The measured magnetic properties are in good agreement with previous studies, further confirming the sample quality.

Electronic structure calculations were performed using the local spin density approximation (LSDA), yielding a ferromagnetic ground state, within the framework of the full potential linear muffin tin orbital method with spin-orbit coupling (46). This approximation has been previously used to study UCoAl (25, 47) and other uranium compounds in the same structural family (48). Experimental lattice constants were used (49), and doping dependence was handled using a rigid band approximation.

Weyl points and other topological features were located and their topology verified in a

single shot method (44). An initial coarse \mathbf{k} -grid of $30 \times 30 \times 30$ was used to locate candidate sources/sinks of Berry curvature flux, whose positions were iteratively refined by repeating the procedure on $2 \times 2 \times 2$ grids within each \mathbf{k} -cube. Additional details can be found in (24).

Transport, thermoelectric, and thermal transport measurements were performed in the same setup. A temperature gradient was generated by a 10 k Ω chip resistor attached to one end of the sample and measured by home-made thermocouples with the calibrated table made of Fe-doped gold and chromel. The other end of the sample was attached to a sapphire substrate that was physically clamped to an oxygen-free copper coldfinger. Conventional steady-state measurements were performed to measure the thermoelectric power and thermal conductivity. The heating power was carefully monitored so that the thermal and thermoelectric responses were linear with the heating power.

-
- [1] L. E. Bell, Cooling, heating, generating power, and recovering waste heat with thermoelectric systems. *Science* **321**, 1457–1461 (2008).
 - [2] J. He, T. M. Tritt, Advances in thermoelectric materials research: Looking back and moving forward. *Science* **357**, eaak9997 (2017).
 - [3] A. Sakai, Y. P. Mizuta, A. A. Nugroho, R. Sihombing, T. Koretsune, M.-T. Suzuki, N. Take-mori, R. Ishii, D. Nishio-Hamane, R. Arita, P. Goswami, S. Nakatsuji, Giant anomalous Nernst effect and quantum-critical scaling in a ferromagnetic semimetal. *Nature Physics* **14**, 1119–1124 (2018).
 - [4] Y. Sakuraba, K. Hasegawa, M. Mizuguchi, T. Kubota, S. Mizukami, T. Miyazaki, K. Takanashi, Anomalous Nernst effect in L10-FePt/MnGa thermopiles for new thermoelectric applications. *Applied Physics Express* **6**, 033003 (2013).
 - [5] N. Nagaosa, J. Sinova, S. Onoda, A. H. MacDonald, N. P. Ong, Anomalous hall effect. *Reviews of modern physics* **82**, 1539 (2010).
 - [6] S. Nakatsuji, N. Kiyohara, T. Higo, Large anomalous Hall effect in a non-collinear antiferromagnet at room temperature. *Nature* **527**, 212–215 (2015).
 - [7] A. K. Nayak, J. E. Fischer, Y. Sun, B. Yan, J. Karel, A. C. Komarek, C. Shekhar, N. Kumar, W. Schnelle, J. Kübler, C. Felser, S. S. P. Parkin, Large anomalous Hall effect driven by a

- nonvanishing Berry curvature in the noncolinear antiferromagnet Mn_3Ge . *Science advances* **2**, e1501870 (2016).
- [8] X. Li, L. Xu, L. Ding, J. Wang, M. Shen, X. Lu, Z. Zhu, K. Behnia, Anomalous Nernst and Righi-Leduc effects in Mn_3Sn : Berry curvature and entropy flow. *Physical review letters* **119**, 056601 (2017).
- [9] M. Ikhlas, T. Tomita, T. Koretsune, M.-T. Suzuki, D. Nishio-Hamane, R. Arita, Y. Otani, S. Nakatsuji, Large anomalous Nernst effect at room temperature in a chiral antiferromagnet. *Nature Physics* **13**, 1085–1090 (2017).
- [10] M. Cutler, N. F. Mott, Observation of Anderson localization in an electron gas. *Physical Review* **181**, 1336 (1969).
- [11] D. Xiao, Y. Yao, Z. Fang, Q. Niu, Berry-phase effect in anomalous thermoelectric transport. *Physical review letters* **97**, 026603 (2006).
- [12] K. Behnia, D. Jaccard, J. Flouquet, On the thermoelectricity of correlated electrons in the zero-temperature limit. *Journal of Physics: Condensed Matter* **16**, 5187 (2004).
- [13] K. Behnia, H. Aubin, Nernst effect in metals and superconductors: a review of concepts and experiments. *Reports on Progress in Physics* **79**, 046502 (2016).
- [14] C. Wuttke, F. Caglieris, S. Sykora, F. Scaravaggi, A. U. Wolter, K. Manna, V. Süß, C. Shekhar, C. Felser, B. Büchner, C. Hess, Berry curvature unravelled by the anomalous Nernst effect in Mn_3Ge . *Physical Review B* **100**, 085111 (2019).
- [15] L. Xu, X. Li, X. Lu, C. Collignon, H. Fu, J. Koo, B. Fauqué, B. Yan, Z. Zhu, K. Behnia, Finite-temperature violation of the anomalous transverse Wiedemann-Franz law. *Science Advances* **6**, eaaz3522 (2020).
- [16] E. Liu, Y. Sun, N. Kumar, L. Muechler, A. Sun, L. Jiao, S.-Y. Yang, D. Liu, A. Liang, Q. Xu, J. Kroder, V. Süß, H. Borrmann, C. Shekhar, Z. Wang, C. Xi, W. Wang, W. Schnelle, S. Wirth, Y. Chen, S. T. B. Goennenwein, C. Felser, Giant anomalous Hall effect in a ferromagnetic kagome-lattice semimetal. *Nature physics* **14**, 1125–1131 (2018).
- [17] T. Kida, L. Fenner, A. Dee, I. Terasaki, M. Hagiwara, A. Wills, The giant anomalous Hall effect in the ferromagnet Fe_3Sn_2 —a frustrated kagome metal. *Journal of Physics: Condensed Matter* **23**, 112205 (2011).
- [18] L. Ye, M. Kang, J. Liu, F. von Cube, C. R. Wicker, T. Suzuki, C. Jozwiak, A. Bostwick, E. Rotenberg, D. C. Bell, L. Fu, R. Comin, J. G. Checkelsky, Massive Dirac fermions in a

- ferromagnetic kagome metal. *Nature* **555**, 638–642 (2018).
- [19] G. Xu, B. Lian, S.-C. Zhang, Intrinsic quantum anomalous hall effect in the kagome lattice $\text{Cs}_2\text{LiMn}_3\text{F}_{12}$. *Physical review letters* **115**, 186802 (2015).
- [20] A. Andreev, L. Havela, V. Sechovsk, M. Bartashevich, J. Šebek, R. Dremov, I. Kozlovskaya, Ferromagnetism in the $\text{UCo}_{1-x}\text{Ru}_x\text{Al}$ quasiternary intermetallics. *Philosophical Magazine B* **75**, 827–844 (1997).
- [21] J. Pospíšil, P. Opletal, M. Vališka, Y. Tokunaga, A. Stunault, Y. Haga, N. Tateiwa, B. Gillon, F. Honda, T. Yamamura, V. Nižňanský, E. Yamamoto, D. Aoki, Properties and Collapse of the Ferromagnetism in $\text{UCo}_{1-x}\text{Ru}_x\text{Al}$ Studied in Single Crystals. *Journal of the Physical Society of Japan* **85**, 034710 (2016).
- [22] P. Veenhuizen, F. De Boer, A. Menovsky, V. Sechovsky, L. Havela, Magnetic properties of URuAl and URhAl single crystals. *Le Journal de Physique Colloques* **49**, C8–485 (1988).
- [23] T. Matsuda, H. Sugawara, Y. Aoki, H. Sato, A. Andreev, Y. Shiokawa, V. Sechovsky, L. Havela, Transport properties of the anisotropic itinerant-electron metamagnet UCoAl . *Physical Review B* **62**, 13852 (2000).
- [24] See supplemental information.
- [25] V. Antonov, B. Harmon, O. Andryushchenko, L. Bekenev, A. N. Yaresko, Electronic structure and x-ray magnetic circular dichroism in uranium compounds. II. UTAl ($T = \text{Co, Rh, and Pt}$) intermetallics. *Physical Review B* **68**, 214425 (2003).
- [26] S.-i. Fujimori, Y. Takeda, T. Okane, Y. Saitoh, A. Fujimori, H. Yamagami, Y. Haga, E. Yamamoto, Y. Ōnuki, Electronic structures of uranium compounds studied by soft x-ray photoelectron spectroscopy. *Journal of the Physical Society of Japan* **85**, 062001 (2016).
- [27] S. Onoda, N. Sugimoto, N. Nagaosa, Quantum transport theory of anomalous electric, thermoelectric, and thermal Hall effects in ferromagnets. *Physical review B* **77**, 165103 (2008).
- [28] L. Xu, X. Li, L. Ding, T. Chen, A. Sakai, B. Fauqué, S. Nakatsuji, Z. Zhu, K. Behnia, Anomalous transverse response of Co_2MnGa and universality of the room-temperature $\alpha_{ij}^A/\sigma_{ij}^A$ ratio across topological magnets. *Physical Review B* **101**, 180404 (2020).
- [29] T. Miyasato, N. Abe, T. Fujii, A. Asamitsu, S. Onoda, Y. Onose, N. Nagaosa, Y. Tokura, Crossover behavior of the anomalous Hall effect and anomalous Nernst effect in itinerant ferromagnets. *Physical review letters* **99**, 086602 (2007).
- [30] L. Ding, J. Koo, L. Xu, X. Li, X. Lu, L. Zhao, Q. Wang, Q. Yin, H. Lei, B. Yan, Z. Zhu,

- K. Behnia, Intrinsic anomalous Nernst effect amplified by disorder in a half-metallic semimetal. *Physical Review X* **9**, 041061 (2019).
- [31] K. Shanavas, Z. S. Popović, S. Satpathy, Theoretical model for Rashba spin-orbit interaction in d electrons. *Physical Review B* **90**, 165108 (2014).
- [32] Y. Hirokane, Y. Tomioka, Y. Imai, A. Maeda, Y. Onose, Longitudinal and transverse thermoelectric transport in MnSi. *Physical Review B* **93**, 014436 (2016).
- [33] F. Herman, S. Skillman, Atomic Structure Calculations (Engelwood Cliffs, NJ (1963).
- [34] D. Xiao, M.-C. Chang, Q. Niu, Berry phase effects on electronic properties. *Reviews of modern physics* **82**, 1959 (2010).
- [35] S.-M. Huang, S.-Y. Xu, I. Belopolski, C.-C. Lee, G. Chang, B. Wang, N. Alidoust, G. Bian, M. Neupane, C. Zhang, S. Jia, A. Bansil, H. Lin, M. Z. Hasan, A Weyl Fermion semimetal with surface Fermi arcs in the transition metal monpnictide TaAs class. *Nature communications* **6**, 1–6 (2015).
- [36] A. A. Soluyanov, D. Gresch, Z. Wang, Q. Wu, M. Troyer, X. Dai, B. A. Bernevig, Type-II weyl semimetals. *Nature* **527**, 495–498 (2015).
- [37] X. Wan, A. M. Turner, A. Vishwanath, S. Y. Savrasov, Topological semimetal and Fermi-arc surface states in the electronic structure of pyrochlore iridates. *Physical Review B* **83**, 205101 (2011).
- [38] H. Weng, C. Fang, Z. Fang, B. A. Bernevig, X. Dai, Weyl semimetal phase in noncentrosymmetric transition-metal monophosphides. *Physical Review X* **5**, 011029 (2015).
- [39] A. Burkov, M. Hook, L. Balents, Topological nodal semimetals. *Physical Review B* **84**, 235126 (2011).
- [40] Y. Du, F. Tang, D. Wang, L. Sheng, E.-j. Kan, C.-G. Duan, S. Y. Savrasov, X. Wan, CaTe: a new topological node-line and Dirac semimetal. *npj Quantum Materials* **2**, 1–4 (2017).
- [41] Y. Kim, B. J. Wieder, C. Kane, A. M. Rappe, Dirac line nodes in inversion-symmetric crystals. *Physical review letters* **115**, 036806 (2015).
- [42] R. Yu, H. Weng, Z. Fang, X. Dai, X. Hu, Topological node-line semimetal and Dirac semimetal state in antiperovskite Cu_3PdN . *Physical review letters* **115**, 036807 (2015).
- [43] Z. Zhu, G. W. Winkler, Q. Wu, J. Li, A. A. Soluyanov, Triple point topological metals. *Physical Review X* **6**, 031003 (2016).
- [44] V. Ivanov, S. Y. Savrasov, Monopole mining method for high-throughput screening for Weyl

- semimetals. *Physical Review B* **99**, 125124 (2019).
- [45] H.-H. Lai, S. E. Grefe, S. Paschen, Q. Si, Weyl–kondo semimetal in heavy-fermion systems. *Proceedings of the National Academy of Sciences* **115**, 93–97 (2018).
- [46] S. Y. Savrasov, Linear-response theory and lattice dynamics: A muffin-tin-orbital approach. *Physical Review B* **54**, 16470 (1996).
- [47] M. Kučera, J. Kuneš, A. Kolomiets, M. Diviš, A. Andreev, V. Sechovský, J.-P. Kappler, A. Rogalev, X-ray magnetic circular dichroism studies of 5 f magnetism in UCoAl and UPtAl. *Physical Review B* **66**, 144405 (2002).
- [48] T. Gasche, S. Auluck, M. Brooks, B. Johansson, Theory of the magnetism of ternary uranium compounds. *Journal of Magnetism and Magnetic Materials* **104**, 37–38 (1992).
- [49] D. Lam, J. Darby Jr, J. Downey, L. Norton, Equiatomic ternary compounds of uranium and aluminium with group viii transition elements. *Journal of Nuclear Materials* **22**, 22–27 (1967).
- [50] T. Gasche, M. Brooks, B. Johansson, Ground-state properties of ternary uranium compounds: I. hybridization effects. *Journal of Physics: Condensed Matter* **7**, 9499 (1995).
- [51] T. Gasche, M. Brooks, B. Johansson, Ground-state properties of ternary uranium compounds: Ii. magnetic properties. *Journal of Physics: Condensed Matter* **7**, 9511 (1995).
- [52] S. Chang, H. Nakotte, A. Andreev, H. Bordallo, L. Havela, V. Sechovsky, M. Torikachvili, Magnetism in some uco 1/3 t 2/3 al solid solutions (t= transition metal). *Journal of Applied Physics* **87**, 6812–6814 (2000).
- [53] S. Chang, H. Nakotte, A. Schultz, H. Bordallo, M. Torikachvili, V. Sechovsky, A. Andreev, Crystallographic order and magnetism in uco1/3t2/3al compounds (t= ru, rh, pt). *Physica B: Condensed Matter* **276**, 634–635 (2000).
- [54] A. Andreev, V. Sechovsky, L. Havela, J. Šebek, M. Bartashevich, T. Goto, K. Kamishima, D. Andreev, V. Gaviko, R. Dremov, *et al.*, Onset of ferromagnetism between the paramagnets ucoal and urual. *Czechoslovak Journal of Physics* **46**, 3385–3386 (1996).
- [55] V. Ivanov, X. Wan, S. Y. Savrasov, Correlation driven topological insulator-to-weyl semimetal transition in actinide system unisn. *arXiv preprint arXiv:1809.09543* (2018).
- [56] A. A. Zyuzin, R. P. Tiwari, Intrinsic anomalous hall effect in type-ii weyl semimetals. *JETP letters* **103**, 717–722 (2016).
- [57] K. Kadowaki, S. Woods, Universal relationship of the resistivity and specific heat in heavy-fermion compounds. *Solid state communications* **58**, 507–509 (1986).

Acknowledgement: We thank Priscila Rosa and Xiangang Wan for useful discussions. The experimental work was performed at Los Alamos National Laboratory under the auspices of the U.S. Department of Energy, Office of Science, Basic Energy Sciences, Materials Sciences and Engineering Division. Theoretical calculations performed by V.I. and S.Y.S. are supported by NSF DMR Grant No. 1832728. T.A. acknowledges support from a LANL LDRD Directors Postdoctoral Fellowship. **Author contributions:** T.A. and F.R. designed the experiment and analyzed the data. T.A., S.M.T., and F.R. built the transport measurement setup. T.A. performed the transport and heat capacity measurements. J.D.T. carried out the magnetic measurements. V.I. and S.Y.S. performed the theoretical calculations. E.D.B. prepared the sample. All authors contributed to writing the manuscript. **Competing interests:** The authors declare that they have no competing interests. **Data and materials availability:** All data needed to evaluate the conclusions in the paper are present in the paper and/or the Supplementary Materials. Additional data related to this paper may be requested from the authors.

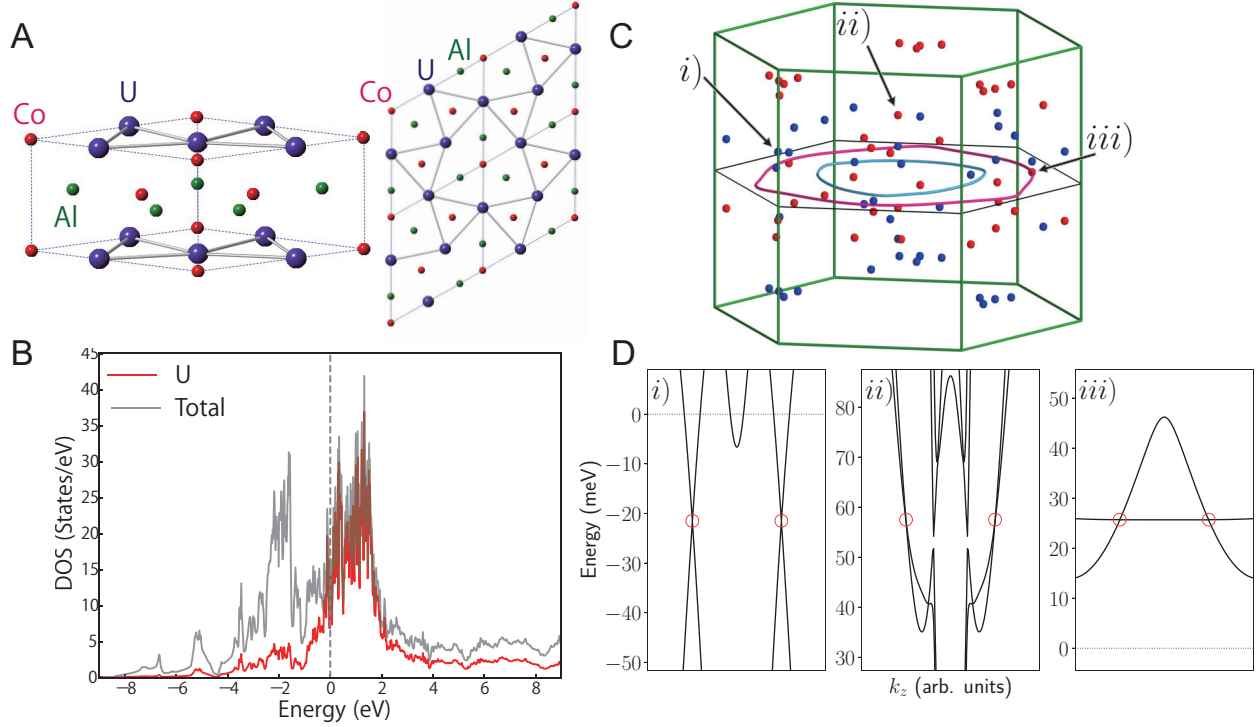


FIG. 1: Crystal structure and theoretical calculations of $\text{UCo}_{0.8}\text{Ru}_{0.2}\text{Al}$. (A) Crystal structure of $\text{UCo}_{1-x}\text{Ru}_x\text{Al}$. (left) The unit cell of UCoAl viewed from the $[111]$ direction. A Co atom is replaced by a Ru atom upon doping. (right) The top view of UCoAl . The solid bonds indicate the tilted kagome layer formed by uranium atoms. (B) Density of states (DOS) including partial DOS for $\text{UCo}_{0.8}\text{Ru}_{0.2}\text{Al}$. (C) Nodal lines and Weyl points within ± 60 meV of the Fermi energy in $\text{UCo}_{0.8}\text{Ru}_{0.2}\text{Al}$. For clarity, Weyl pairs with a k_z separation $< 0.2 \cdot 2\pi/c$ are not shown. (D) Band plots for examples of i) Type-I, ii) Type-II and iii) critically tilted Weyl points (red circles), identified with arrows in (C), plotted on the interval $-2k_W < k_z < 2k_W$, where $2k_W$ is the Weyl pair separation along the k_z direction.

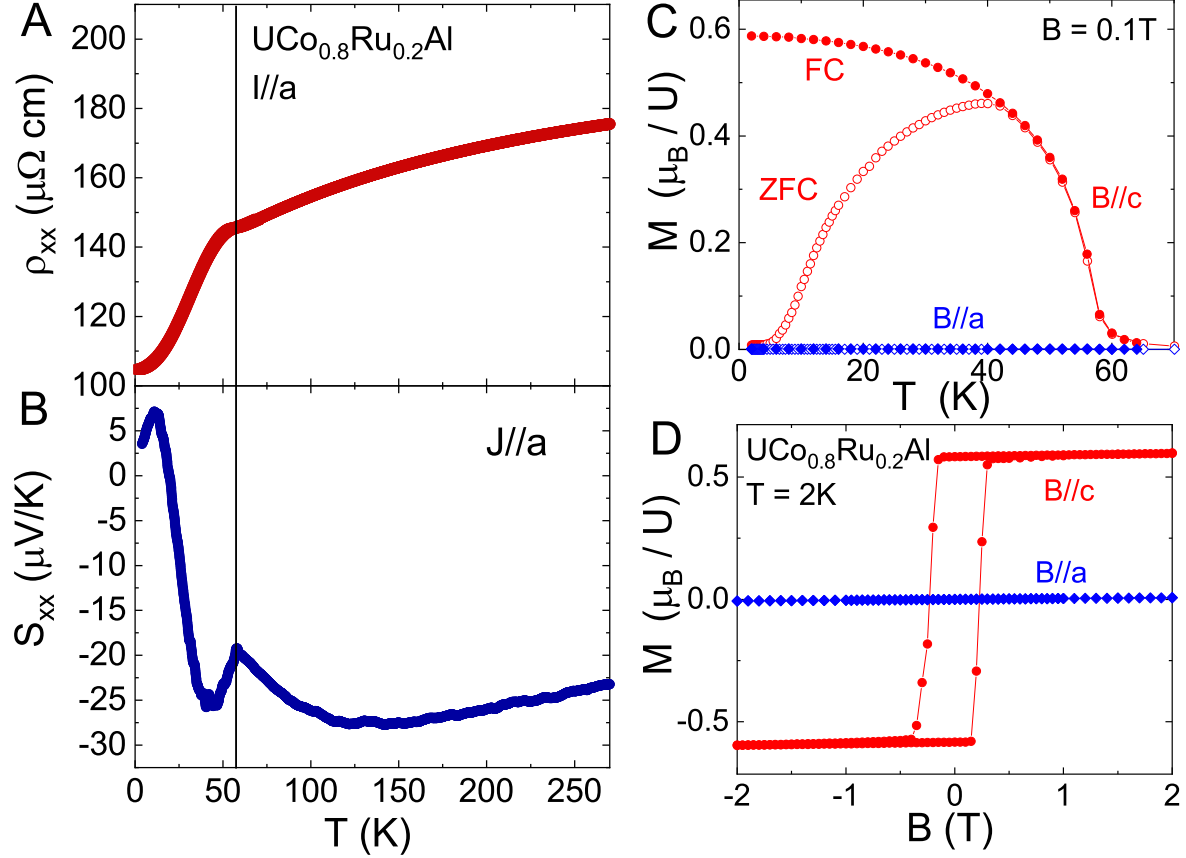


FIG. 2: Longitudinal transport and magnetization properties of single crystalline $\text{UCo}_{0.8}\text{Ru}_{0.2}\text{Al}$. (A) Electrical resistivity ρ vs. temperature T with the current $I \parallel a$. The vertical solid line indicates the ferromagnetic critical temperature. (B) Seebeck coefficient S_{xx} vs. T with the heat current $J \parallel a$. (C) Temperature dependence of the magnetization M per formula unit for $B \parallel c$ (red) and $B \parallel a$ (blue) in an applied field $B = 0.1 \text{ T}$. (D) Field dependence of the magnetization $M(H)$ at $T = 2 \text{ K}$.

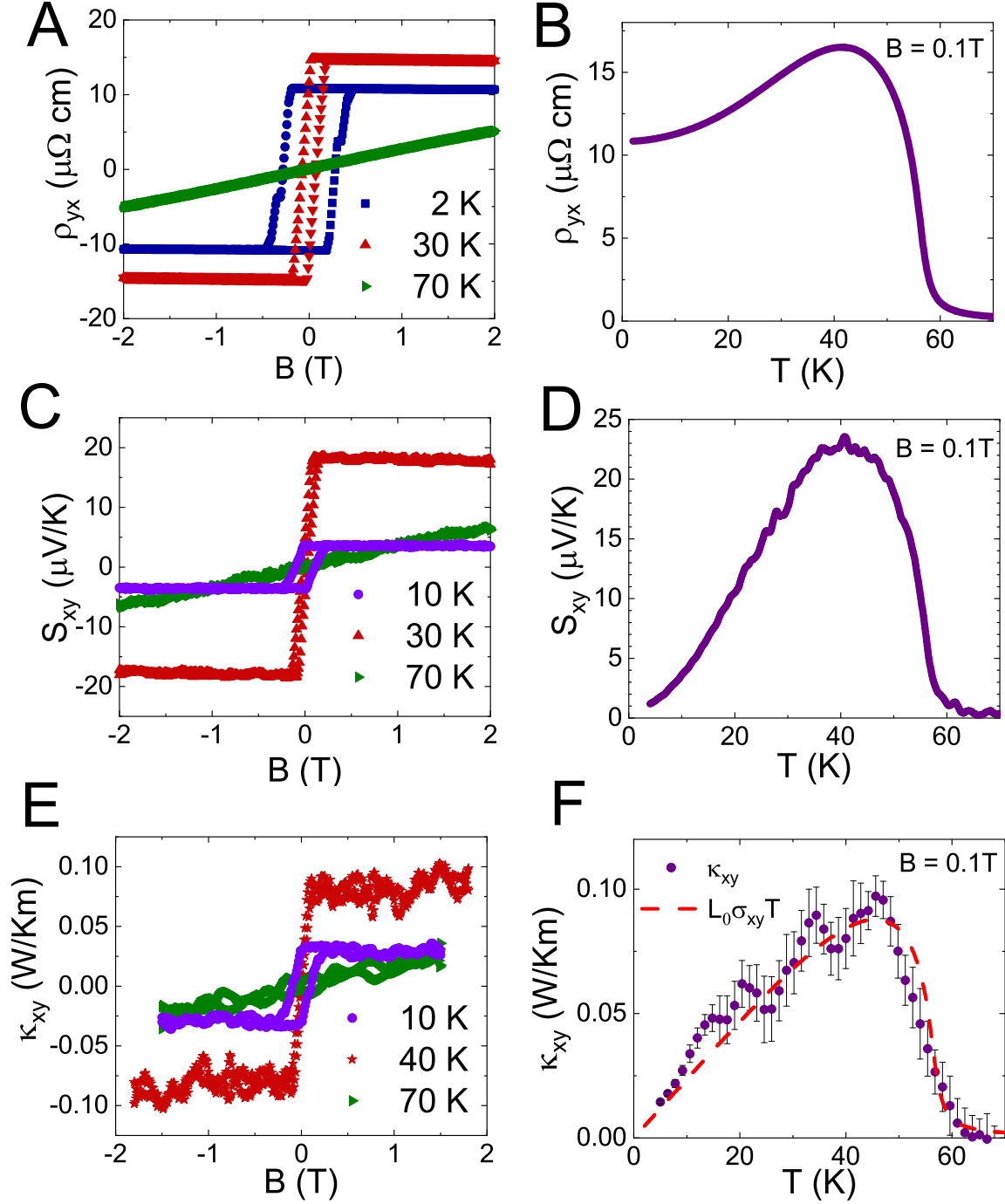


FIG. 3: Colossal anomalous transverse responses from $\text{UCo}_{0.8}\text{Ru}_{0.2}\text{Al}$ with $B \parallel c$. (A)(B) Hall effect ρ_{xy} as a function of magnetic field B and temperature T , respectively. (C)(D) Nernst effect S_{xy} as a function of B and T , respectively. (E)(F) Thermal Hall (Righi–Leduc) effect κ_{xy} as a function of B and T , respectively. The red dashed line in (F) is the expected thermal Hall conductivity based on the electrical Hall conductivity if the Wiedemann-Franz law is satisfied. All temperature dependent data were taken with $B = 0.1$ T.

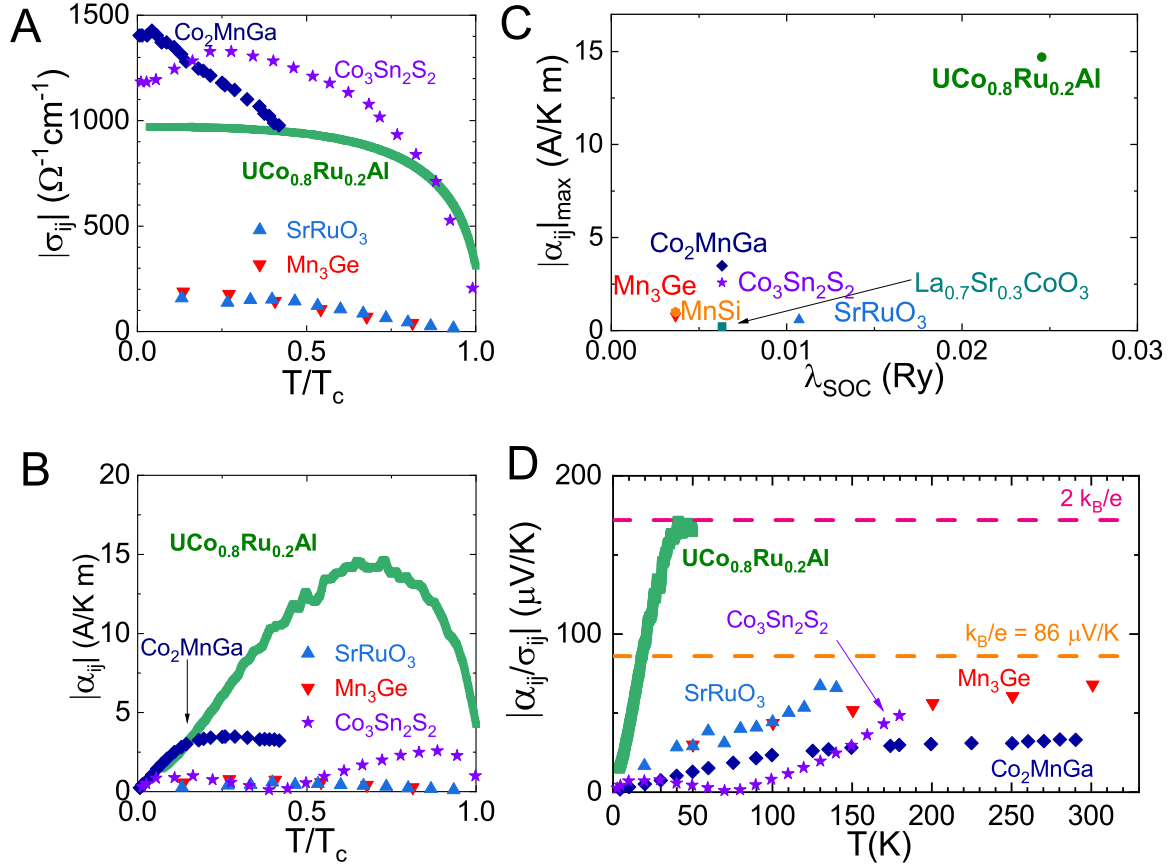


FIG. 4: Anomalous Hall and Peltier conductivity of various magnets. (A) Anomalous Hall conductivity σ_{ij} and (B) Anomalous Peltier conductivity α_{ij} as a function of normalized temperature T/T_c (green line). For comparison, other materials with large anomalous contributions are also shown. (C) The maximum value of α_{ij} for various compounds compared with the strength of the spin-orbit coupling of the magnetic element (31). The compounds include $\text{UCo}_{0.8}\text{Ru}_{0.2}\text{Al}$ (this work, green circle), Co_2MnGa (blue diamond) (28), $\text{Co}_3\text{Sn}_2\text{S}_2$ (purple star) (30), SrRuO_3 (29) (cyan upper triangle), LSCO (light green square) (29), Mn_3Ge (red lower triangle) (15), and MnSi (orange hexagon) (32). (D) Plot of α_{ij}/σ_{ij} versus T . Orange and pink dashed lines indicate k_B/e and $2k_B/e$, respectively.

Colossal anomalous Nernst effect in correlated noncentrosymmetric kagome ferromagnet

T. Asaba^{1*}, V. Ivanov², S. M. Thomas¹, S.Y. Savrasov², J. D. Thompson¹, E. D. Bauer¹, F. Ronning^{3*}

¹*Materials Physics and Applications Division,
Los Alamos National Laboratory, NM, 87545 USA*

²*Department of Physics,
University of California,
Davis, CA 95616, USA*

³*Institute for Materials Science,
Los Alamos National Laboratory, NM, 87545 USA*

(Dated: April 20, 2021)

arXiv:2104.09060v1 [cond-mat.str-el] 19 Apr 2021

I. COMPUTATIONAL DETAILS

To obtain the electronic structure of doped $\text{UCo}_{0.8}\text{Ru}_{0.2}\text{Al}$, we performed a series of electronic structure calculations within the framework of the full potential linear muffin tin orbital method with spin-orbit coupling (45), using the local spin density approximation (LSDA), which has been previously employed to study uranium compounds with the ZrNiAl -type structure (47, 50, 51).

To assess the effect of chemical substitution on the electronic structure, we perform calculations for the parent compound UCoAl , as well as doped at the $x = 1/3, 2/3$ and 1 levels, using the experimental lattice parameters. The UTAl ($T=\text{Co,Ru}$) structure has two inequivalent sites for atom T, T_1 and T_2 , with Ru preferentially occupying the two T_2 sites (52, 53). Therefore calculations on the chemically ordered compounds $\text{UCo}_{2/3}\text{Ru}_{1/3}\text{Al}$, $\text{UCo}_{1/3}\text{Ru}_{2/3}\text{Al}$ with Ru at the T_2 site will give a representative picture of the doping effects on the electronic structure of $\text{UCo}_{1-x}\text{Ru}_x\text{Al}$. The resulting band structures are shown below.

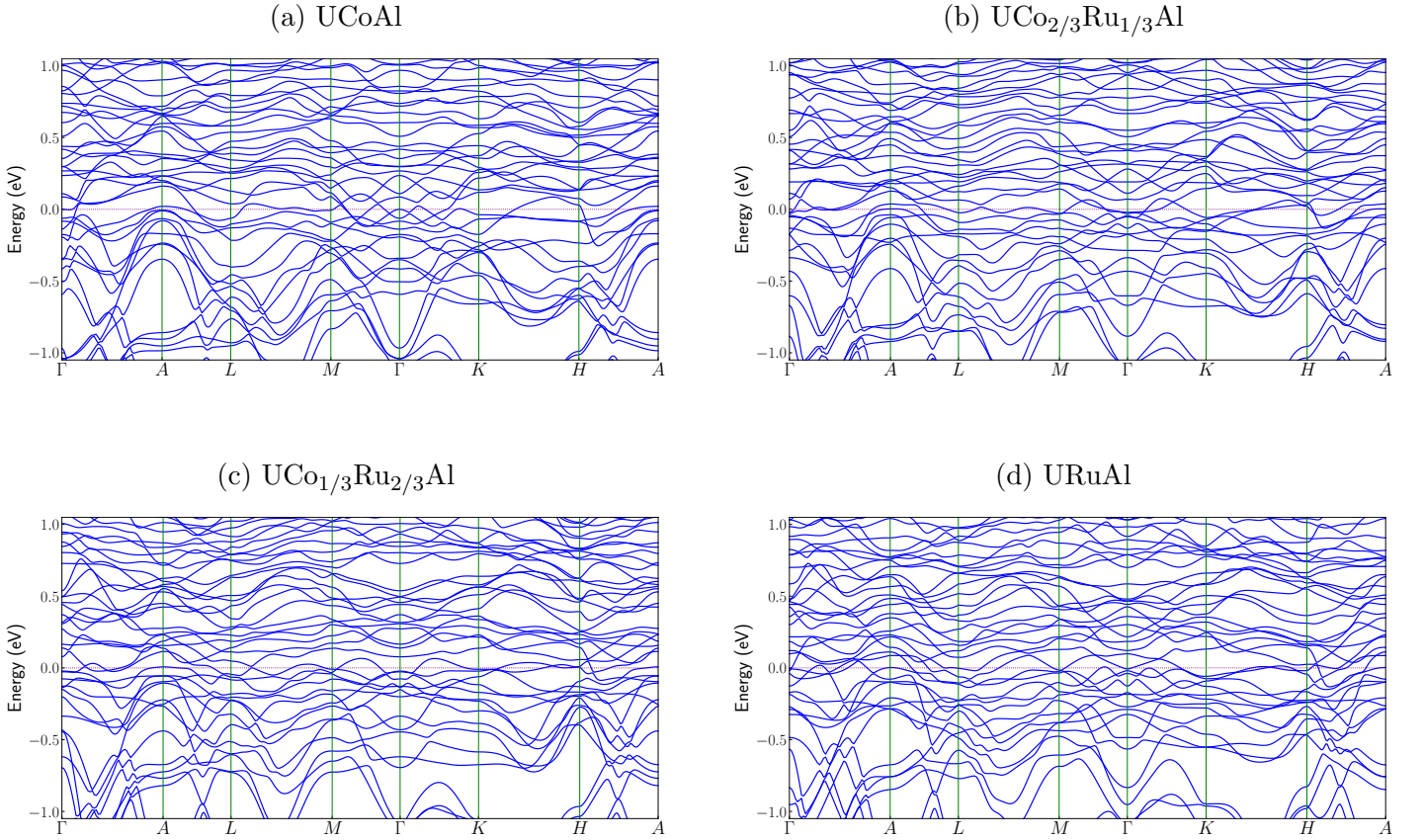


FIG. S1: **Calculated band structures of chemically ordered members of the $\text{UCo}_{1-x}\text{Ru}_x\text{Al}$ series.** Computed band structures for the stoichiometric compounds in the $\text{UCo}_{1-x}\text{Ru}_x\text{Al}$ series, with $x = 0, 1/3, 2/3, 1$. $E_F = 0$ is the Fermi level corresponding to the $x = 0.2$ doping.

Figure S1 shows that as Ru is substituted for Co, the band structure remains largely unchanged, aside from a downward shift in the Fermi level due to the removal of electrons. These calculations indicate that a rigid band approximation for doped $\text{UCo}_{1-x}\text{Ru}_x\text{Al}$ is appropriate. Consequently, to approximate the electronic structure of $\text{UCo}_{0.8}\text{Ru}_{0.2}\text{Al}$, we use the electronic structure of pure UCoAl with a rigid band shift up of 41.04 meV corresponding to the $x = 0.2$ doping level. This will be used consistently throughout the manuscript and the supplement.

The uranium f -orbitals reside on a kagome lattice. Thus, the effects of frustrated hopping on such a lattice and the small spatial extent of the 5f orbitals will be intermixed. Identifying specific bands associated with the kagome structure is further complicated by the multiorbital nature of uranium, the presence of ligand orbitals, and the three dimensionality of the structure. Nevertheless, multiple flat bands can be observed in the bandstructure plots of Fig. S1. One would expect the flat bands near the Fermi energy to be renormalized by electronic correlations present in this system.

For UCoAl , the computed orbital $\mu_l = 1.19\mu_B$ and spin $\mu_s = -0.98\mu_B$ magnetic moments, which are similar to those found in prior calculations (46). Experimentally $\text{UCo}_{1-x}\text{Ru}_x\text{Al}$ is paramagnetic for $x = 0$, developing a static magnetic moment in the doping range $x = 0.005 - 0.78$, with a maximum uranium magnetic moment $\mu_U = 0.6\mu_B$ around $x = 0.3$ (54). Therefore, with the appropriate adjustment of Fermi level, our calculated electronic structure for UCoAl is a reasonable model to compare with experimental observations for doped $\text{UCo}_{0.8}\text{Ru}_{0.2}\text{Al}$. It is important to note that our model is only valid at energies corresponding to dopings within the magnetic range, and not for the paramagnetic end points. We further emphasize that while details of the actual electronic structure may vary, the main observation of an abundance of topological features close to E_F will be insensitive to all detailed variations of the electronic structure.

II. IDENTIFICATION OF TOPOLOGICAL FEATURES

To understand the origin of the large anomalous Hall- and anomalous Nernst effects in $\text{UCo}_{0.8}\text{Ru}_{0.2}\text{Al}$, we perform a previously developed mining procedure (43) to find topological features in the electronic structure. Because the topological features closest to the Fermi level will be the most relevant to the transport properties, we scanned the range of energies $E_F \pm 60\text{meV}$ for topological features.

We divide the Brillouin zone (BZ) into an initial coarse k -grid of $30 \times 30 \times 30$ divisions, and compute the Berry curvature flux through the surface of each k -cube. This grid is subsequently refined by iteratively repeating the search procedure on a $2 \times 2 \times 2$ grid within each k -cube until the desired precision is achieved. This allows us to find the locations of sources/sinks of Berry curvature flux,

simultaneously confirming the topological nature of the features as well as their positions in k -space. Our procedure reveals a number of topological features in $\text{UCo}_{0.8}\text{Ru}_{0.2}\text{Al}$, including Weyl points, nodal lines, and triple points. The triple points (42) only exist within the paramagnetic state, and therefore, will not be discussed in this manuscript. Both Weyl nodes and nodal lines exist in the ferromagnetic state.

The Weyl points we identify in $\text{UCo}_{0.8}\text{Ru}_{0.2}\text{Al}$ are summarized in Table I, and fall into one of three general classes. The main two types of Weyl points we term Weyl-A' and Weyl-B', due to their relationship to the Weyl-A and Weyl-B types of Weyl points we have identified for compounds with the ZrNiAl-type structure (43).

For reference, Weyl points belonging to type Weyl-A form six pairs found along the $\Gamma - M$ line and are separated along the k_z direction. Weyl-B points are instead 12 pairs which are found in sets of four, symmetrically displaced from the $\Gamma - K$ line. The reason for 12 Weyl points being the minimum number can be understood in terms of a symmetry argument. While Weyl points can arise due to the absence of either time-reversal \mathcal{T} or inversion \mathcal{I} symmetries, here they exist due to broken inversion. Now, while $\mathcal{T}(\mathbf{k}) = -\mathbf{k}$, the topological charge of a Weyl point is invariant under \mathcal{T} . This means that a positively charged Weyl point located at \mathbf{k} will have a positively charged partner at $-\mathbf{k}$, each of which will have a negatively charged partner across the σ_z mirror plane as shown in Fig S2a. In combination with the three-fold symmetry of the BZ, this guarantees that each Weyl point belongs to a symmetry-related set with a number of members that is a multiple of twelve.

In $\text{UCo}_{1-x}\text{Ru}_x\text{Al}$, the uranium magnetic moments break \mathcal{T} -symmetry on top of the already absent inversion symmetry of the lattice. This means that the inversion symmetry $\mathbf{k} \leftrightarrow -\mathbf{k}$ in \mathbf{k} -space is fully broken, splitting the Weyl A and Weyl B types each into two sets of Weyl A' or Weyl B' types, with 6 and 12 members respectively (Fig S2c). This can be understood as a direct consequence of the Zeeman-like effect shifting the bands, causing the k_z -separation between Weyl point partners to increase or decrease (Fig S2b). A similar mechanism can create lone pairs of Weyl points along the $\Gamma - A$ axis, separated only along the k_z direction (55). Since this sort of Weyl point is pinned to the k_z -axis, application of point group symmetries does not yield any new symmetry-related members. Therefore these sets have only two members, which is the minimum for materials with broken \mathcal{T} -symmetry.

Band	Location	Type	#	δk_z	v (Ry/ \hat{k})	C (Ry/ \hat{k})	E(meV)
71	(0.00000, 0.33057, 0.02756)	Weyl-A'	6	0.0030000	-0.0418333	0.0183333	-63
71	(0.00000,-0.53900, 0.09977)	Weyl-A'	6	0.0268000	-0.0549254	0.0107090	-30
71	(0.00000, 0.15877, 0.12084)	Weyl-A'	6	0.0174000	-0.0427011	-0.0177299	-15
71	(0.00000,-0.45758,-0.12498)	Weyl-A'	6	0.0317400	0.0811122	-0.0017171	-22
71	(0.00000, 0.55407, 0.22190)	Weyl-A'	6	0.0178400	-0.0225897	0.0070348	-6
71	(0.61459, 0.05412,-0.12708)	Weyl-B'	12	0.0304600	0.0391005	0.0207814	-51
71	(0.41976, 0.10908,-0.42260)	Weyl-B'	12	0.0112000	0.0174554	-0.0062946	-32
71	(0.00000, 0.31823,-0.45537)	Weyl-A'	6	0.0112000	0.0132366	-0.0018973	-44
71	(0.00000,-0.38203, 0.38948)	Weyl-A'	6	0.0240000	-0.0208750	0.0056250	+2
72	(0.00000, 0.38736, 0.00434)	Weyl-A'	6	0.0040000	-0.0842500	0.0823750	-51
72	(0.00000, 0.51091,-0.01959)	Weyl-A'	6	0.0078000	0.0377885	-0.0377884	+26
72	(0.00000,-0.07528,-0.03239)	Weyl-A'	6	0.0049560	0.0329903	-0.0069613	-23
72	(0.27505,-0.00369, 0.03266)	Weyl-B'	12	0.0030000	-0.0510833	0.0505833	-32
72	(0.00000, 0.08053, 0.02120)	Weyl-A'	6	0.0048000	-0.0233333	0.0063542	-28
72	(0.00000, 0.23693,-0.05635)	Weyl-A'	6	0.0126000	0.1351587	0.1173413	-1
72	(0.00000,-0.18377, 0.09803)	Weyl-A'	6	0.0130000	-0.1004615	0.0413462	+28
72	(0.40132,-0.13379,-0.13770)	Weyl-B'	12	0.0130000	0.0300000	0.0206538	+59
72	(0.00000, 0.00000, 0.22577)	k_z	2	0.0210000	-0.0063095	0.0300238	+57

TABLE I: **Weyl points of $\text{UCo}_{0.8}\text{Ru}_{0.2}\text{Al}$.** The first column gives the lower band number of two bands comprising the Weyl point. The second column gives the position of one positive charge given for each symmetry-related set of Weyl points. The third and fourth columns give the classification of the Weyl points as Weyl-A', Weyl-B', or k_z , and the number of symmetry-related Weyl points in the set. The remaining columns give the momentum cutoff δk_z , velocities v and C , and energy E , of each

Weyl point. Wavevectors \mathbf{k} are given in units of $2\pi/a, 2\pi/a, 2\pi/c$.

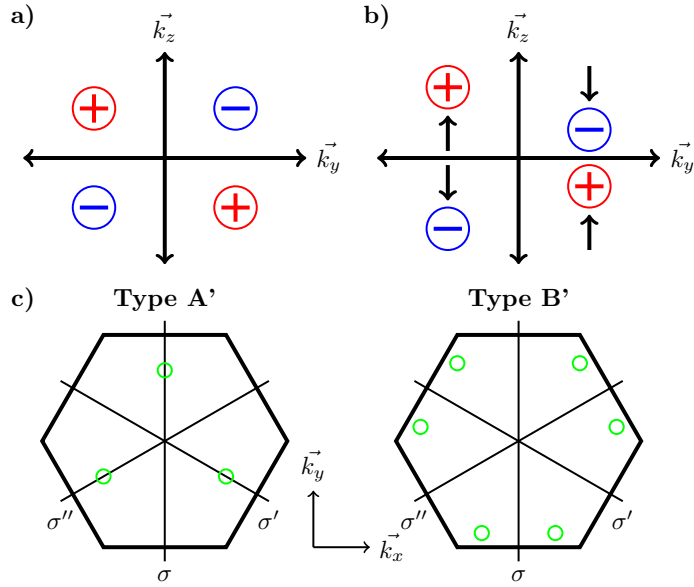


FIG. S2: Schematics showing how breaking $\vec{k} \leftrightarrow -\vec{k}$ symmetry splits Weyl points in the ZrNiAl-type structure. a) 4 Type-A Weyl points in $\text{UCo}_{1-x}\text{Ru}_x\text{Al}$ in the absence of magnetism. b) Turning on the magnetic field breaks $\mathbf{k} \leftrightarrow -\mathbf{k}$ symmetry, splitting the original set of Weyl points into two sets of Type A' or Type B'. c) Symmetries of Type A' and Type B' Weyl points in $\text{UCo}_{1-x}\text{Ru}_x\text{Al}$, as seen from above.

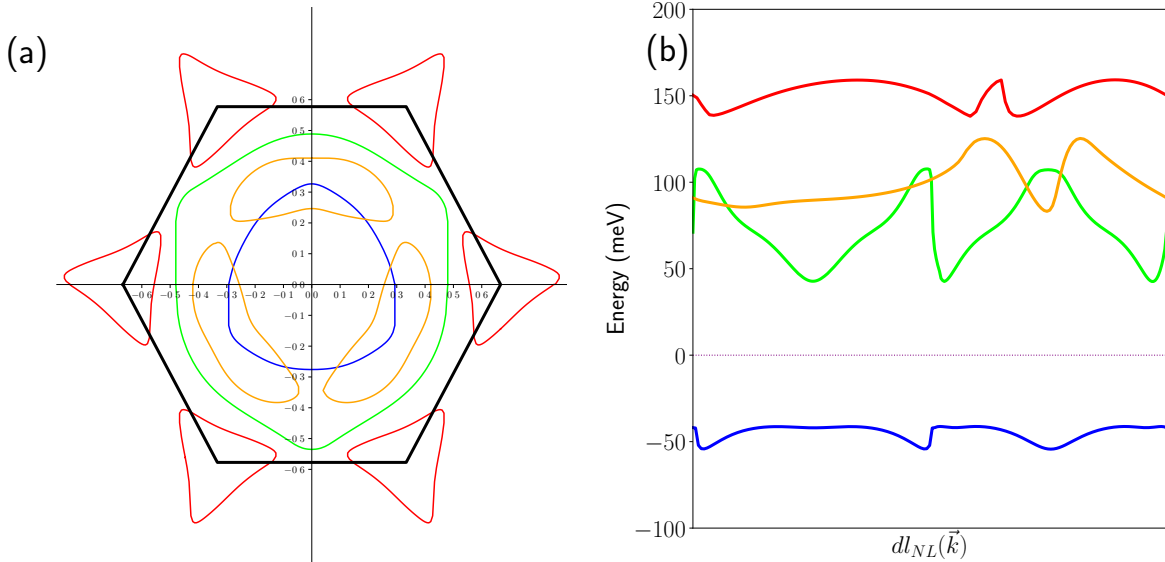


FIG. S3: Nodal lines of $\text{UCo}_{0.8}\text{Ru}_{0.2}\text{Al}$. a) Nodal lines within the σ_z plane of $\text{UCo}_{0.8}\text{Ru}_{0.2}\text{Al}$. b) Nodal lines plotted as a function of energy.

In addition to the Weyl points we find a number of topological nodal lines in the electronic structure of $\text{UCo}_{0.8}\text{Ru}_{0.2}\text{Al}$, shown in Figure S3a. This type of nodal line can arise at the intersection of two bands belonging to two different irreducible representations of the mirror plane point group. In

UCo_{1-x}Ru_xAl, these nodal lines have different eigenvalues when acted upon by the σ_z mirror plane. As a result the band degeneracy at their intersection point is topologically protected against small distortions. These nodal lines are located at least 50 meV above/below the Fermi energy (Fig S3b). While they occupy a larger part of the topological phase space than the Weyl points, they likely don't make a significant contribution to the Berry curvature at the Fermi energy of the $x = 0.2$ doped case. Specifically, the nodal lines lying within the σ_z plane will not contribute to Ω_{xy}^z and hence will not impact σ_{xy} or α_{xy} .

III. WEYL MODEL

The large number of topological features in UCo_{0.8}Ru_{0.2}Al result in a dense population of singularities in the Berry curvature. This means that the standard approach for computing anomalous Hall and anomalous Nernst effects would require dense \mathbf{k} -grids that are too large to be computationally tractable. Instead, we take a pragmatic approach by using a solvable model for each pair of identified Weyl points, allowing us to practically compute the anomalous Hall and Nernst effects.

We can construct an effective model using the positions of the Weyl points in UCo_{1-x}Ru_xAl, and the velocity parameters extracted from the local band structure near the Weyl points (parameters listed in Table I). The simplest such model simply assigns a plateau of anomalous hall conductivity $\sigma_{xy} = e^2 Q / 2\pi^2 \hbar$ to each Weyl point within some momentum cutoff range. However, several of the Weyl points are strongly tilted, which affects their contribution to the AHC, so we will use an extended model which takes this tilt into account (56):

$$\begin{aligned} H(\mathbf{k})_+ &= +\hbar C(k_z - Q) - \hbar v \boldsymbol{\sigma} \cdot (\mathbf{k} - Q \hat{k}_z) \\ H(\mathbf{k})_- &= -\hbar C(k_z + Q) + \hbar v \boldsymbol{\sigma} \cdot (\mathbf{k} + Q \hat{k}_z) \end{aligned} \quad (1)$$

which describes two Weyl points with chirality ± 1 separated by a distance $2Q$ in momentum space along the \hat{k}_z direction. For the velocity units used in Table I, $\hbar = 1$, but is included here for clarity. In this sign convention, positive v describes a negatively charged Weyl point at $k = Q$, and a positive Weyl point at $k = -Q$. Changing the sign of v interchanges the two Weyl points. The parameter C controls the tilting of the Weyl cones, with positive C describing a tilting of the Weyl cones *inward* towards $k_z = 0$, and negative C corresponding to both cones tilting *outward*, away from $k_z = 0$:

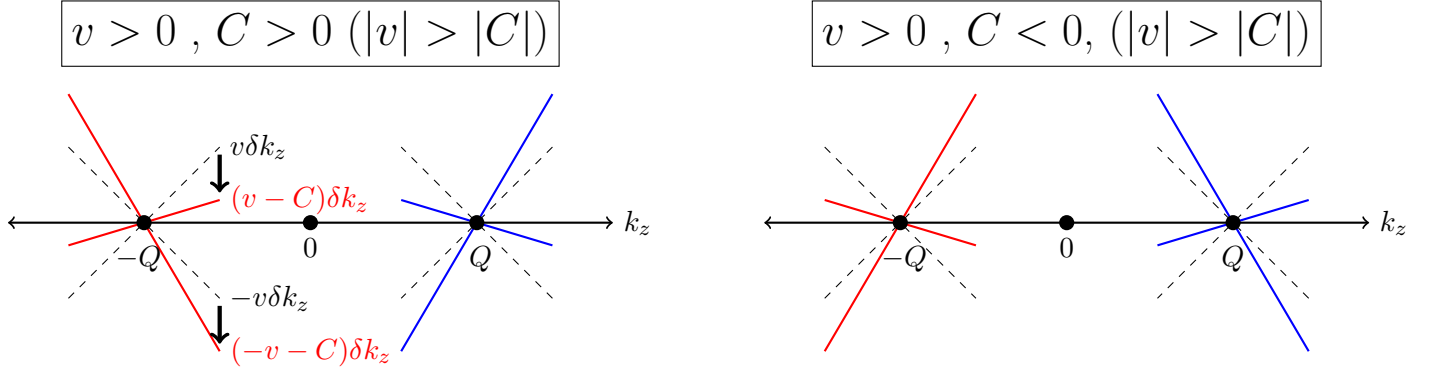


FIG. S4: Type-I Weyl points.

In the figure above, the dashed lines, denote untitled Type-I cones (second terms in equation 1). Taking the C -dependent terms into account tilts the Weyl cones. By increasing C until it exceeds the Fermi velocity $|C| > |v|$, the Weyl cones can be tilted below the horizontal, transitioning from Type-I to Type-II Weyl points:

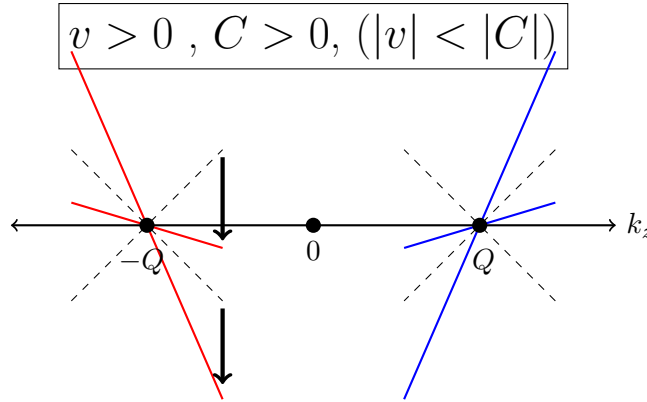


FIG. S5: Type-II Weyl points.

For this model, the anomalous Hall contribution in the limit of zero temperature, can be written:

$$\begin{aligned}
\sigma_{xy} = & -\frac{e^2}{8\pi^2} \int_{\Lambda-Q}^{-\Lambda+Q} dk_z \left[\text{sign}(k_z) \theta(v^2 k_z^2 - (Ck_z - (\epsilon - \epsilon_W))^2) \right. \\
& \left. + \frac{vk_z}{|Ck_z - (\epsilon - \epsilon_W)|} (1 - \theta(v^2 k_z^2 - (Ck_z - (\epsilon - \epsilon_W))^2)) \right] \\
& + \frac{e^2}{8\pi^2} \int_{\Lambda+Q}^{-\Lambda-Q} dk_z \left[\text{sign}(k_z) \theta(v^2 k_z^2 - (-Ck_z - (\epsilon - \epsilon_W))^2) \right. \\
& \left. + \frac{vk_z}{|-Ck_z - (\epsilon - \epsilon_W)|} (1 - \theta(v^2 k_z^2 - (-Ck_z - (\epsilon - \epsilon_W))^2)) \right]
\end{aligned} \tag{2}$$

where e_W is the energy at which the Weyl point is located, $\theta(x)$ is the Heaviside step function, and Λ is an effective momentum cutoff. The first integral in the expression is the contribution from the Weyl at $k_z = Q$, and the second is from the Weyl at $k_z = -Q$. The terms in the first integral can be understood as a contribution of $vk_z/|Ck_z - (\epsilon - \epsilon_W)|$ when $-\mu/(V - C) < k_z < mu/(V + C)$ and $\text{sign}(k_z)$ otherwise (flip signs for terms in the second integral).

In turn, the anomalous Nernst effect can be computed from the zero-temperature anomalous Hall through the following formula (11):

$$\begin{aligned}\alpha(T, \mu) &= -\frac{1}{e} \int d\epsilon \left(\frac{\partial f_{\text{FD}}}{\partial \mu} \right) \sigma(0, \epsilon) \frac{\epsilon - \mu}{T} = -\frac{1}{e} \int d\epsilon \frac{e^{(\epsilon - \mu)/(k_B T)}}{k_B T (e^{(\epsilon - \mu)/(k_B T)} + 1)^2} \sigma(0, \epsilon) \frac{\epsilon - \mu}{T} \\ &= -\frac{1}{eT} \int w\left(\frac{\epsilon - \mu}{k_B T}\right) \sigma(0, \epsilon) d\epsilon\end{aligned}\quad (3)$$

where f_{FD} is the Fermi-Dirac distribution, and $w(x) = xe^x/(e^x + 1)^2$ is a weight function introduced to simplify the expression.

The computed anomalous Hall effect for the Weyl points listed in Table I is shown in Figure S6a. A large value of σ_{xy} appears just above the Fermi level, suggesting that a collective contribution from several Weyl points could explain the large experimentally observed values. This plot must be interpreted very carefully for a number of reasons. Firstly, the anomalous Hall contribution for each pair of Weyl points depends on their k_z separation, which in turn depends on the uranium magnetic moments. As we have previously mentioned, these are difficult to reproduce numerically. Secondly, while we take a relatively dense initial grid of $30 \times 30 \times 30$ k-points to search for topological features, the dense distribution of the Weyl points we found suggests the possibility that some initial k -cubes may contain multiple Weyl points, meaning there may be yet more additional Weyl points missed by our procedure. Thirdly, this calculation does not include contributions from nodal lines and other sources. Finally, $\text{UCo}_{1-x}\text{Ru}_x\text{Al}$ is magnetic for dopings $x = 0.005 - 0.78$, so outside of this range, our model would not apply.

We also draw attention to the anomalous Hall effect contribution coming from the Weyl point located at (0.0, 0.51, -0.02) and 26 meV above the Fermi energy (and its symmetry related partners) (Fig S6b),c). The anomalous Nernst contribution of these points is computed by setting the chemical potential at +26 meV and evaluating the above integral. This set of Weyl points is close to a Lifshitz transition between Type-I and Type-II tilting. For tilted Weyl points near the Lifshitz transition, $\partial\sigma_{xy}/\partial\epsilon$ diverges logarithmically at the critical tilt, resulting in large anomalous Hall and Nernst effects, as well as an amplification of α_{xy} relative to σ_{xy} (3). In UCoAl , these Weyl points are located +26 meV above the Fermi energy, corresponding to a doping of $x = 0.07$, and are sufficient to explain the large anomalous Hall (~ 1200 [Ohm cm] $^{-1}$), large anomalous Nernst (~ 20 A/K m), and a α_{xy}/σ_{xy} ratio which exceeds k_B/e observed in this material.

We reiterate that the Weyl points in this material, along with their associated Berry curvature and other observable properties, are sensitive to the uranium magnetic moments and additional electronic renormalization effects. This means that in the undoped case, the absence of magnetism would guarantee a zero anomalous Hall effect, even though Fig S6a suggests a large value. Additionally, as it is difficult to exactly reproduce the uranium magnetic moment μ_U , the critical set of Weyl points identified above may be located at a lower energy corresponding to the $x = 0.2$ doping level.

A final consideration is that the magnetism in $\text{UCo}_{1-x}\text{Ru}_x\text{Al}$ disappears at higher temperatures, meaning the anomalous Nernst effect will rapidly go to zero as it approaches the magnetic transition.

To summarize, our calculations yield a large number of topological features, including Weyl points, triple points, and nodal lines. Some Weyl nodes are sufficient to explain the the large anomalous Hall and anomalous Nernst observed in $\text{UCo}_{0.8}\text{Ru}_{0.2}\text{Al}$. Additional calculations and measurements are needed to identify which features are most responsible.

IV. MEASUREMENT SETUP

Fig. S7 shows the transport measurement setup. A resistor is attached to the sample as a heater, generating the heat flow. The other end is glued to the sapphire substrate via silver epoxy. The low-thermal conductivity phosphor-bronze copper wires were attached to the sample and heater to minimize the heat dissipation through the electrical leads. Home-made gold-iron and chromel thermocouples were calibrated and used to measure the temperature gradient in the linear response regime. We define our coordinates as shown in red in Fig. S7. The heat and current flow is along the x direction, which is

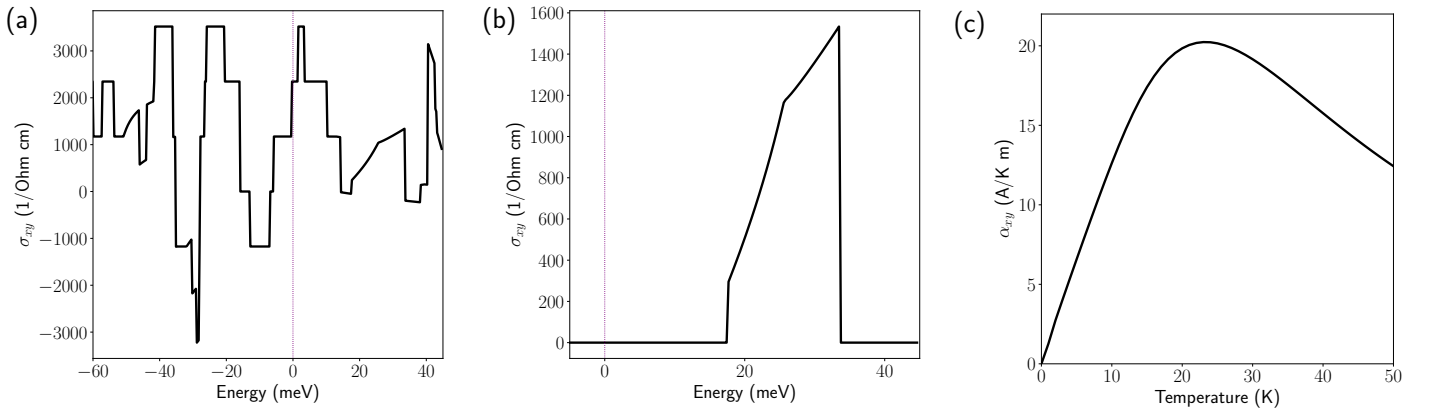


FIG. S6: **Calculated anomalous Hall effect and anomalous Nernst effects for $\text{UCo}_{0.8}\text{Ru}_{0.2}\text{Al}$.** a) Anomalous Hall effect computed for all Weyl points in $\text{UCo}_{0.8}\text{Ru}_{0.2}\text{Al}$. b) The anomalous Hall effect for set of Weyl points at +26 meV c) The anomalous Nernst effect as a function of temperature computed with the chemical potential set at +26 meV.

also parallel to the a -axis of the crystal. y and z are parallel to the a^* - and the c -axis of the crystal, respectively.

The electric and heat currents follow the equations below.

$$J_e = \sigma E - \alpha \nabla T \quad (4)$$

$$J_q = T \alpha E - \kappa \nabla T \quad (5)$$

where J_e and J_q are electron and heat flow, σ , α and κ are conductivity, thermoelectric (Peltier) and thermal conductivity tensors, and E is the electric field, respectively. In Eq. 5, the first term on the right hand side is negligible compared to the second term for our sample. Therefore, the expressions for the thermal conductivity are $\kappa_{xx} = -J_q \nabla_x T / ((\nabla_x T)^2 + (\nabla_y T)^2)$ and $\kappa_{xy} = -J_q \nabla_y T / ((\nabla_x T)^2 + (\nabla_y T)^2)$ where $\nabla_y T = +\Delta T_y / w$ with $\Delta T_y = (T_1 - T_2)$ and $\nabla_x T = -\Delta T_x / w$ with $\Delta T_x = (T_{hot} - T_{cold})$ being the temperature drop along the length of the sample in the x direction. As shown in Fig. S8, we find $\kappa_{xy} \ll \kappa_{xx}$ and therefore $\Delta T_y \ll \Delta T_x$. In this setup the electrical current is zero (ie. $J_e = 0$). By defining the thermoelectric tensor $S \equiv \rho \alpha$ where ρ is resistivity tensor, we obtain

$$E_x = S_{xx} \nabla_x T + S_{xy} \nabla_y T \quad (6)$$

$$E_y = -S_{xy} \nabla_x T + S_{yy} \nabla_y T. \quad (7)$$

Given that $\Delta T_y \ll \Delta T_x$ and $S_{xx} \approx S_{yy}$, these equations further reduce to $S_{xx} = -E_x l / \Delta T_x$ and $S_{xy} = E_y l / \Delta T_x$, which is our definition of the Seebeck and Nernst effects.

In our coordinate, the Nernst effect takes the modern convention and is defined as S_{xy} as $-(V1 - V2)l / \Delta T_x w$, where the Hall effect is defined as $\rho_{xy} = (V1 - V2)t / I_x$. Here $V1$ and $V2$ are the voltages measured at the points shown in cyan in the figure, I_x is the current along the x direction. l , w , and t are the length, width and thickness of the sample, respectively. In both cases, the positive field is applied along the z direction.

V. TWO COMPONENTS OF THE PELTIER COEFFICIENT α

The Peltier coefficient is the sum of two terms $\alpha_{xy} = \alpha_1 + \alpha_2$ with $\alpha_1 = S_{xx} \sigma_{xy}$ and $\alpha_2 = S_{xy} \sigma_{xx}$. Fig. S9 shows the temperature dependence of α_1 and α_2 . The latter component is almost one order of magnitude larger than the former one at $T = 41$ K, dominating the Peltier coefficient. This is one of the significant features of $\text{UCo}_{0.8}\text{Ru}_{0.2}\text{Al}$, as most known materials are dominated by $S_{xx} \sigma_{xy}$.

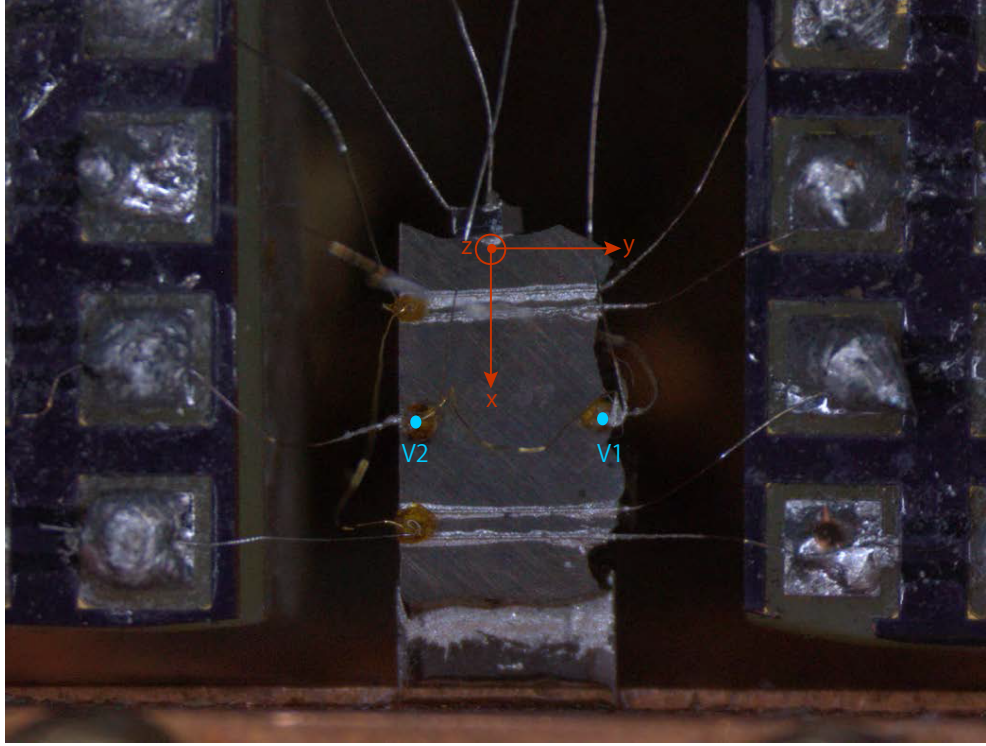


FIG. S7: **Photograph of our experimental setup.** The magnetic field is applied parallel to c -axis.

Photo credit: T. Asaba (Los Alamos National Laboratory).

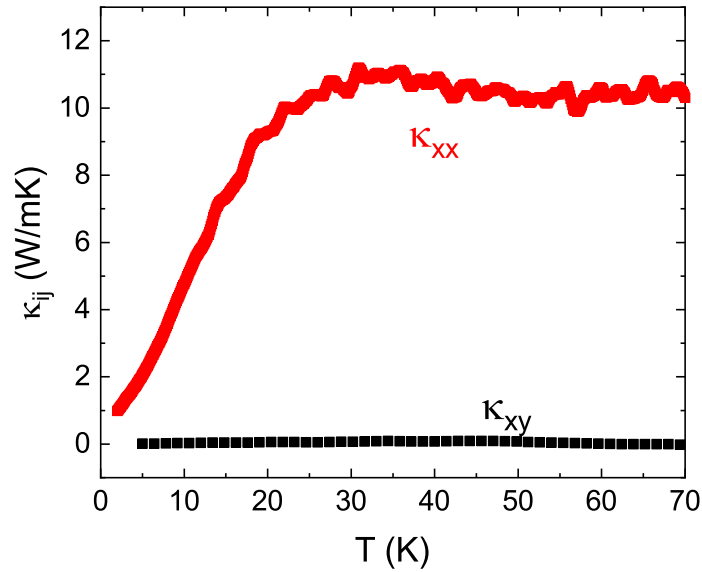


FIG. S8: **Thermal conductivity of $\text{UCo}_{0.8}\text{Ru}_{0.2}\text{Al}$.** Longitudinal (red) and transverse (black) thermal conductivity as a function of temperature.

VI. SPECIFIC HEAT MEASUREMENTS

The low-temperature specific heat measurement data is shown in Fig. S10. The specific heat over temperature is plotted as a function of temperature squared. The Sommerfeld coefficient $\gamma=41$

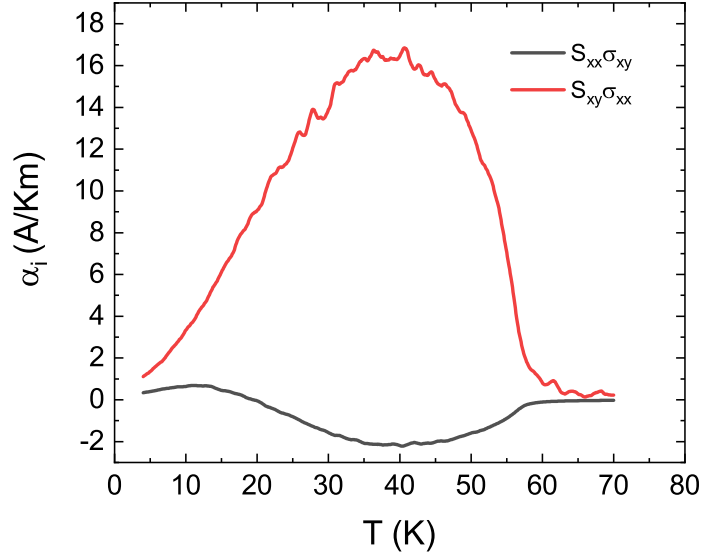


FIG. S9: **Two Peltier components.** Two components of $\alpha_{xy}=\alpha_1+\alpha_2=S_{xx}\sigma_{xy}+S_{xy}\sigma_{xx}$ are shown as a function of temperature.

mJ/mol-U K² indicates that the system is moderately correlated. The Fermi temperature, $T_F = E_F/k_B$ is estimated by the equation (12)

$$\gamma = \frac{\pi^2 k_B^2 n}{2E_F} \quad (8)$$

where γ is the Sommerfeld coefficient in units of J/K²m³, k_B is Boltzmann's constant and n is the carrier density. Here, we assume that there is one carrier per unit cell. The estimated Fermi temperature is 930 K. The density of states computed from our LSDA calculations is shown in Fig. 1 of the main text. From this the computed Sommerfeld coefficient can be obtained $\gamma_{band} = (\pi^2 k_B^2/3)N_{LSDA}(0) = 13$ mJ/mol-U K². A comparison with the experimental γ gives a mass enhancement of ~ 3 .

We also calculated the Kadowaki-Woods ratio A/γ^2 , where A is the T^2 coefficient of resistivity. A is obtained by the quadratic fitting of resistivity as shown in Fig. S11. The obtained value of A is 2.26×10^{-8} $\Omega\text{cm}/\text{K}^2$. Accordingly, A/γ^2 of $\text{UCo}_{0.8}\text{Ru}_{0.2}\text{Al}$ is estimated to be 1.3×10^{-5} ($\mu\Omega\text{cm}/\text{K}^2$)/(mJ/mol K²)², which is close to the universal value of $\sim 1 \times 10^{-5}$ ($\mu\Omega\text{cm}/\text{K}^2$)/(mJ/mol K²)² (57).

VII. SEEBECK EFFECT AT LOW TEMPERATURES

Similarly, the Fermi temperature is estimated from S/T at the zero temperature limit through the equation (12)

$$S/T = \frac{\pi^2 k_B}{2eT_F} \quad (9)$$

where e is the charge of an electron. S/T in the $T=0$ limit is $0.9 \mu\text{V}/\text{K}^2$ giving an estimated Fermi temperature of 470 K. Also, the positive thermopower at zero temperature limit indicates that hole-like

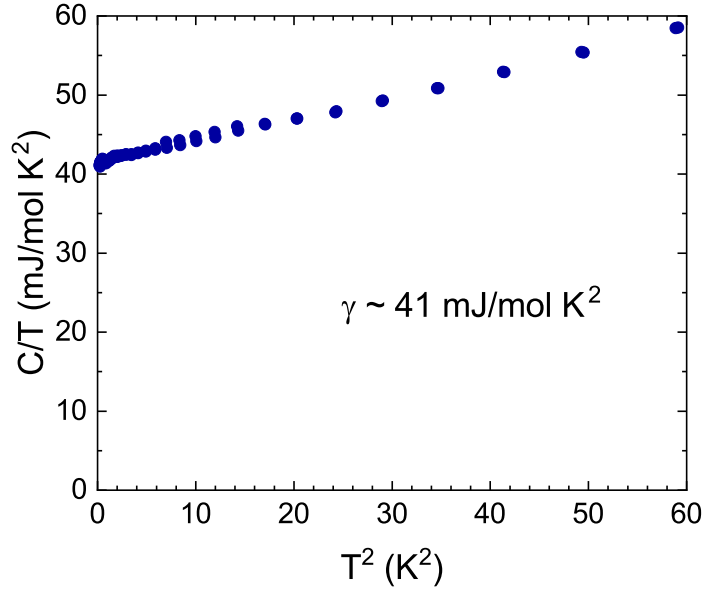


FIG. S10: **The C/T as a function of temperature squared T^2 .** The extrapolated value of C/T to $T=0$ gives the Sommerfeld coefficient $\gamma=41 \text{ mJ/mol K}^2$.

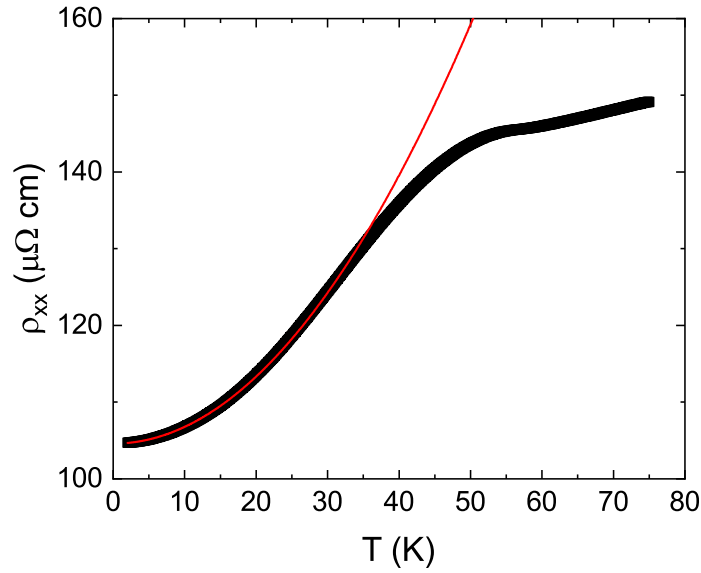


FIG. S11: **The low temperature resistivity vs temperature plot.** The red line is a quadratic fit to $\rho = \rho_0 + AT^2$ up to 15 K resulting in $A = 2.26 \times 10^{-8} \Omega\text{cm/K}^2$.

carriers dominate the thermoelectric transport at low temperatures.

-
- [1] L. E. Bell, Cooling, heating, generating power, and recovering waste heat with thermoelectric systems. *Science* **321**, 1457–1461 (2008).
- [2] J. He, T. M. Tritt, Advances in thermoelectric materials research: Looking back and moving forward. *Science* **357**, eaak9997 (2017).
- [3] A. Sakai, Y. P. Mizuta, A. A. Nugroho, R. Sihombing, T. Koretsune, M.-T. Suzuki, N. Takemori, R. Ishii, D. Nishio-Hamane, R. Arita, P. Goswami, S. Nakatsuji, Giant anomalous Nernst effect and quantum-critical scaling in a ferromagnetic semimetal. *Nature Physics* **14**, 1119–1124 (2018).
- [4] Y. Sakuraba, K. Hasegawa, M. Mizuguchi, T. Kubota, S. Mizukami, T. Miyazaki, K. Takanashi, Anomalous Nernst effect in L10-FePt/MnGa thermopiles for new thermoelectric applications. *Applied Physics Express* **6**, 033003 (2013).
- [5] N. Nagaosa, J. Sinova, S. Onoda, A. H. MacDonald, N. P. Ong, Anomalous hall effect. *Reviews of modern physics* **82**, 1539 (2010).
- [6] S. Nakatsuji, N. Kiyohara, T. Higo, Large anomalous Hall effect in a non-collinear antiferromagnet at room temperature. *Nature* **527**, 212–215 (2015).
- [7] A. K. Nayak, J. E. Fischer, Y. Sun, B. Yan, J. Karel, A. C. Komarek, C. Shekhar, N. Kumar, W. Schnelle, J. Kübler, C. Felser, S. S. P. Parkin, Large anomalous Hall effect driven by a nonvanishing Berry curvature in the noncolinear antiferromagnet Mn_3Ge . *Science advances* **2**, e1501870 (2016).
- [8] X. Li, L. Xu, L. Ding, J. Wang, M. Shen, X. Lu, Z. Zhu, K. Behnia, Anomalous Nernst and Righi-Leduc effects in Mn_3Sn : Berry curvature and entropy flow. *Physical review letters* **119**, 056601 (2017).
- [9] M. Ikhlas, T. Tomita, T. Koretsune, M.-T. Suzuki, D. Nishio-Hamane, R. Arita, Y. Otani, S. Nakatsuji, Large anomalous Nernst effect at room temperature in a chiral antiferromagnet. *Nature Physics* **13**, 1085–1090 (2017).
- [10] M. Cutler, N. F. Mott, Observation of Anderson localization in an electron gas. *Physical Review* **181**, 1336 (1969).
- [11] D. Xiao, Y. Yao, Z. Fang, Q. Niu, Berry-phase effect in anomalous thermoelectric transport. *Physical review letters* **97**, 026603 (2006).
- [12] K. Behnia, D. Jaccard, J. Flouquet, On the thermoelectricity of correlated electrons in the zero-temperature limit. *Journal of Physics: Condensed Matter* **16**, 5187 (2004).
- [13] K. Behnia, H. Aubin, Nernst effect in metals and superconductors: a review of concepts and experiments. *Reports on Progress in Physics* **79**, 046502 (2016).

- [14] C. Wuttke, F. Caglieris, S. Sykora, F. Scaravaggi, A. U. Wolter, K. Manna, V. Süß, C. Shekhar, C. Felser, B. Büchner, C. Hess, Berry curvature unravelled by the anomalous Nernst effect in Mn_3Ge . *Physical Review B* **100**, 085111 (2019).
- [15] L. Xu, X. Li, X. Lu, C. Collignon, H. Fu, J. Koo, B. Fauqué, B. Yan, Z. Zhu, K. Behnia, Finite-temperature violation of the anomalous transverse Wiedemann-Franz law. *Science Advances* **6**, eaaz3522 (2020).
- [16] E. Liu, Y. Sun, N. Kumar, L. Muechler, A. Sun, L. Jiao, S.-Y. Yang, D. Liu, A. Liang, Q. Xu, J. Kroder, V. Süß, H. Borrmann, C. Shekhar, Z. Wang, C. Xi, W. Wang, W. Schnelle, S. Wirth, Y. Chen, S. T. B. Goennenwein, C. Felser, Giant anomalous Hall effect in a ferromagnetic kagome-lattice semimetal. *Nature physics* **14**, 1125–1131 (2018).
- [17] T. Kida, L. Fenner, A. Dee, I. Terasaki, M. Hagiwara, A. Wills, The giant anomalous Hall effect in the ferromagnet Fe_3Sn_2 —a frustrated kagome metal. *Journal of Physics: Condensed Matter* **23**, 112205 (2011).
- [18] L. Ye, M. Kang, J. Liu, F. von Cube, C. R. Wicker, T. Suzuki, C. Jozwiak, A. Bostwick, E. Rotenberg, D. C. Bell, L. Fu, R. Comin, J. G. Checkelsky, Massive Dirac fermions in a ferromagnetic kagome metal. *Nature* **555**, 638–642 (2018).
- [19] G. Xu, B. Lian, S.-C. Zhang, Intrinsic quantum anomalous hall effect in the kagome lattice $\text{Cs}_2\text{LiMn}_3\text{F}_{12}$. *Physical review letters* **115**, 186802 (2015).
- [20] A. Andreev, L. Havela, V. Sechovsk, M. Bartashevich, J. Šebek, R. Dremov, I. Kozlovskaya, Ferromagnetism in the $\text{UCo}_{1-x}\text{Ru}_x\text{Al}$ quasiternary intermetallics. *Philosophical Magazine B* **75**, 827–844 (1997).
- [21] J. Pospíšil, P. Opletal, M. Vališka, Y. Tokunaga, A. Stunault, Y. Haga, N. Tateiwa, B. Gillon, F. Honda, T. Yamamura, V. Nižňanský, E. Yamamoto, D. Aoki, Properties and Collapse of the Ferromagnetism in $\text{UCo}_{1-x}\text{Ru}_x\text{Al}$ Studied in Single Crystals. *Journal of the Physical Society of Japan* **85**, 034710 (2016).
- [22] P. Veenhuizen, F. De Boer, A. Menovsky, V. Sechovsky, L. Havela, Magnetic properties of URuAl and URhAl single crystals. *Le Journal de Physique Colloques* **49**, C8–485 (1988).
- [23] T. Matsuda, H. Sugawara, Y. Aoki, H. Sato, A. Andreev, Y. Shiokawa, V. Sechovsky, L. Havela, Transport properties of the anisotropic itinerant-electron metamagnet UCoAl . *Physical Review B* **62**, 13852 (2000).
- [24] See supplemental information.
- [25] V. Antonov, B. Harmon, O. Andryushchenko, L. Bekenev, A. N. Yaresko, Electronic structure and x-ray magnetic circular dichroism in uranium compounds. II. UTAl ($T = \text{Co}, \text{Rh}, \text{and Pt}$) intermetallics. *Physical Review B* **68**, 214425 (2003).
- [26] S.-i. Fujimori, Y. Takeda, T. Okane, Y. Saitoh, A. Fujimori, H. Yamagami, Y. Haga, E. Yamamoto, Y. Ōnuki, Electronic structures of uranium compounds studied by soft x-ray photoelectron spectroscopy. *Journal of the Physical Society of Japan* **85**, 062001 (2016).

- [27] S. Onoda, N. Sugimoto, N. Nagaosa, Quantum transport theory of anomalous electric, thermoelectric, and thermal Hall effects in ferromagnets. *Physical review B* **77**, 165103 (2008).
- [28] L. Xu, X. Li, L. Ding, T. Chen, A. Sakai, B. Fauqué, S. Nakatsuji, Z. Zhu, K. Behnia, Anomalous transverse response of Co₂MnGa and universality of the room-temperature $\alpha_{ij}^A/\sigma_{ij}^A$ ratio across topological magnets. *Physical Review B* **101**, 180404 (2020).
- [29] T. Miyasato, N. Abe, T. Fujii, A. Asamitsu, S. Onoda, Y. Onose, N. Nagaosa, Y. Tokura, Crossover behavior of the anomalous Hall effect and anomalous Nernst effect in itinerant ferromagnets. *Physical review letters* **99**, 086602 (2007).
- [30] L. Ding, J. Koo, L. Xu, X. Li, X. Lu, L. Zhao, Q. Wang, Q. Yin, H. Lei, B. Yan, Z. Zhu, K. Behnia, Intrinsic anomalous Nernst effect amplified by disorder in a half-metallic semimetal. *Physical Review X* **9**, 041061 (2019).
- [31] K. Shanavas, Z. S. Popović, S. Satpathy, Theoretical model for Rashba spin-orbit interaction in *d* electrons. *Physical Review B* **90**, 165108 (2014).
- [32] F. Herman, S. Skillman, Atomic Structure Calculations (Engelwood Cliffs, NJ (1963).
- [33] D. Xiao, M.-C. Chang, Q. Niu, Berry phase effects on electronic properties. *Reviews of modern physics* **82**, 1959 (2010).
- [34] S.-M. Huang, S.-Y. Xu, I. Belopolski, C.-C. Lee, G. Chang, B. Wang, N. Alidoust, G. Bian, M. Neupane, C. Zhang, S. Jia, A. Bansil, H. Lin, M. Z. Hasan, A Weyl Fermion semimetal with surface Fermi arcs in the transition metal monpnictide TaAs class. *Nature communications* **6**, 1–6 (2015).
- [35] A. A. Soluyanov, D. Gresch, Z. Wang, Q. Wu, M. Troyer, X. Dai, B. A. Bernevig, Type-II weyl semimetals. *Nature* **527**, 495–498 (2015).
- [36] X. Wan, A. M. Turner, A. Vishwanath, S. Y. Savrasov, Topological semimetal and Fermi-arc surface states in the electronic structure of pyrochlore iridates. *Physical Review B* **83**, 205101 (2011).
- [37] H. Weng, C. Fang, Z. Fang, B. A. Bernevig, X. Dai, Weyl semimetal phase in noncentrosymmetric transition-metal monophosphides. *Physical Review X* **5**, 011029 (2015).
- [38] A. Burkov, M. Hook, L. Balents, Topological nodal semimetals. *Physical Review B* **84**, 235126 (2011).
- [39] Y. Du, F. Tang, D. Wang, L. Sheng, E.-j. Kan, C.-G. Duan, S. Y. Savrasov, X. Wan, CaTe: a new topological node-line and Dirac semimetal. *npj Quantum Materials* **2**, 1–4 (2017).
- [40] Y. Kim, B. J. Wieder, C. Kane, A. M. Rappe, Dirac line nodes in inversion-symmetric crystals. *Physical review letters* **115**, 036806 (2015).
- [41] R. Yu, H. Weng, Z. Fang, X. Dai, X. Hu, Topological node-line semimetal and Dirac semimetal state in antiperovskite Cu₃PdN. *Physical review letters* **115**, 036807 (2015).

- [42] Z. Zhu, G. W. Winkler, Q. Wu, J. Li, A. A. Soluyanov, Triple point topological metals. *Physical Review X* **6**, 031003 (2016).
- [43] V. Ivanov, S. Y. Savrasov, Monopole mining method for high-throughput screening for Weyl semimetals. *Physical Review B* **99**, 125124 (2019).
- [44] H.-H. Lai, S. E. Grefe, S. Paschen, Q. Si, Weyl-kondo semimetal in heavy-fermion systems. *Proceedings of the National Academy of Sciences* **115**, 93–97 (2018).
- [45] S. Y. Savrasov, Linear-response theory and lattice dynamics: A muffin-tin-orbital approach. *Physical Review B* **54**, 16470 (1996).
- [46] M. Kučera, J. Kuneš, A. Kolomiets, M. Diviš, A. Andreev, V. Sechovský, J.-P. Kappler, A. Rogalev, X-ray magnetic circular dichroism studies of 5 f magnetism in UCoAl and UPtAl. *Physical Review B* **66**, 144405 (2002).
- [47] T. Gasche, S. Auluck, M. Brooks, B. Johansson, Theory of the magnetism of ternary uranium compounds. *Journal of Magnetism and Magnetic Materials* **104**, 37–38 (1992).
- [48] D. Lam, J. Darby Jr, J. Downey, L. Norton, Equiatomic ternary compounds of uranium and aluminium with group viii transition elements. *Journal of Nuclear Materials* **22**, 22–27 (1967).
- [49] Y. Hirokane, Y. Tomioka, Y. Imai, A. Maeda, Y. Onose, Longitudinal and transverse thermoelectric transport in MnSi. *Physical Review B* **93**, 014436 (2016).
- [50] T. Gasche, M. Brooks, B. Johansson, Ground-state properties of ternary uranium compounds: I. hybridization effects. *Journal of Physics: Condensed Matter* **7**, 9499 (1995).
- [51] T. Gasche, M. Brooks, B. Johansson, Ground-state properties of ternary uranium compounds: II. magnetic properties. *Journal of Physics: Condensed Matter* **7**, 9511 (1995).
- [52] S. Chang, H. Nakotte, A. Andreev, H. Bordallo, L. Havela, V. Sechovsky, M. Torikachvili, Magnetism in some uco 1/3 t 2/3 al solid solutions (t= transition metal). *Journal of Applied Physics* **87**, 6812–6814 (2000).
- [53] S. Chang, H. Nakotte, A. Schultz, H. Bordallo, M. Torikachvili, V. Sechovsky, A. Andreev, Crystallographic order and magnetism in uco1/3t2/3al compounds (t= ru, rh, pt). *Physica B: Condensed Matter* **276**, 634–635 (2000).
- [54] A. Andreev, V. Sechovsky, L. Havela, J. Šebek, M. Bartashevich, T. Goto, K. Kamishima, D. Andreev, V. Gaviko, R. Dremov, *et al.*, Onset of ferromagnetism between the paramagnets ucoal and ureal. *Czechoslovak Journal of Physics* **46**, 3385–3386 (1996).
- [55] V. Ivanov, X. Wan, S. Y. Savrasov, Correlation driven topological insulator-to-weyl semimetal transition in actinide system unisn. *arXiv preprint arXiv:1809.09543* (2018).

- [56] A. A. Zyuzin, R. P. Tiwari, Intrinsic anomalous hall effect in type-ii weyl semimetals. *JETP letters* **103**, 717–722 (2016).
- [57] K. Kadowaki, S. Woods, Universal relationship of the resistivity and specific heat in heavy-fermion compounds. *Solid state communications* **58**, 507–509 (1986).